8-5-2010

Creation, Verification, and Validation of a Panel Code for the Analysis of Ship Propellers in a Steady, Uniform Wake

Stephen Gregory Jennings
University of New Orleans

Creation, Verification, and Validation of a Panel Code for the Analysis of Ship Propellers in a Steady, Uniform Wake

A Thesis

Submitted to the Graduate Faculty of the
University of New Orleans
in partial fulfillment of the
requirements for the degree of

Master of Science
in
Engineering
Naval Architecture and Marine Engineering

by

Stephen Gregory Jennings
B.S., University of New Orleans, 2006

August, 2010

Acknowledgments

First, I would like to thank my wife Katie for her unwaivering support during my long nights at the computer.

I would also like to thank Dr. Lothar Birk, who's guidance in research and writing was always helpful and supportive.

Finally, I want to express my gratitude for the finacial support provided by Northrop Grumman Shipbuilding.

Contents

List of Figures

List of Tables

List of Symbols

$\Delta\phi$	Potential difference across wake surface
Ω	Rotational speed of the propeller
Φ	Velocity potential
α	Angle from free stream direction
$\chi(r')$	Blade rake as a function of r'
$\epsilon(\epsilon_{max}, e_{max}, e)$	Camber of the blade
$\epsilon_{max}(r')$	Maximum camber of the a radial blade section, function of r'
η	Parametric variable in panel shape function
$\gamma(r')$	Blade pitch angle as a function of r'
ϕ	Perturbation velocity potential
ϕ_j	Perturbation velocity potential at panel j
ϕ_+	Potential on the suction side of the wake
ϕ_-	Potential on the pressure side of the wake
$\phi_{\pm j}$	Perturbation potential at the center of the suction(+) or pressure(-) side trailing edge panels of the jth spanwise strip
$\tau(\tau_{max}, e)$	Half thickness of the blade
τ_{max}	Maximum thickness of a radial blade section, function of r'
θ	Angle in $P - xr\theta$
$\theta_k(k)$	Angular location of the blade midchord at the hub of blade k
$\xi(r')$	Blade skew as a function of r'
ζ	Parametric variable in panel shape function

$\mathbf{\Delta}\phi$	Vector of perturbation potential differences around the trailing edge
$\mathbf{\Delta V}$	Vector of velocity magnitude differences around the trailing edge
$\mathbf{BP}(r', e, k)$	Location of blade pressure face surface
$\mathbf{BS}(r', e, k)$	Location of blade suction face surface
$\mathbf{c}$	Unit vector in the$Pn - cs$ coordinate system described in the $P - xyz$ coordinate system
$\mathbf{MC}(r', k)$	Location of blade mid-chord line
$\mathbf{n_Q}$	Surface normal vector at point $\mathbf{Q}$
$\mathbf{NT}(r', k, e)$	Location of blade nose-tail line
$\mathbf{n}$	Surface normal vector
$\mathbf{o}$	Unit vector of the $Pn - op$ Cartesian coordinate system described in the $P - xyz$ coordinate system
$\mathbf{P}(\mathbf{x}, \mathbf{y}, \mathbf{z})$	Arbitrary field point
$\mathbf{p}$	Unit vector of the $Pn - op$ Cartesian coordinate system described in the $P - xyz$ coordinate system
$\mathbf{Q}$	Vector locating a point on the surface S
$\mathbf{q}_0$, $\mathbf{q}_1$, $\mathbf{q}_2$, & $\mathbf{q}_3$	Coefficients of panel shape function
$\mathbf{q}_{++}$, $\mathbf{q}_{+-}$, $\mathbf{q}_{-+}$, & $\mathbf{q}_{--}$	Panel corner locations
$\mathbf{R_{ijk}}$	Vector pointing from influenced panel i to influencing panel j on blade k
$\mathbf{R}$	$= \mathbf{Q} - \mathbf{P}$
$\mathbf{s}$	Unit vector in the$Pn - cs$ coordinate system described in the $P - xyz$ coordinate system
$\mathbf{V_{inf}}$	Free stream velocity
$\mathbf{V_I}$	Incident velocity on the propeller blade surface
a	Coefficient of $\phi_c(g)$ or $\phi_s(g)$
b	Coefficient of $\phi_c(g)$ or $\phi_s(g)$

B_{ij}	Influencing potential on panel i from source distribution on panel(s) j
c	Coefficient of $\phi_c(g)$ or $\phi_s(g)$
$C(r')$	Blade chord as a function of r'
C_P	Pressure coefficient
C_{ij}	Influencing potential on panel i from doublet distribution on panel(s) j
E	Constant used in (2.8)
e	Non-dimensional, unit chord, such that 0 is the leading edge and 1 is the trailing edge
$e_{max}(r')$	Location where the maximum camber occurs along the nose-tail line, function of r'
f	Variable in (3.3)
g	Distance along the blade surface
g_{++}	Distance from the center of the panel of interest to panel $m+2$
$g_{\pm}$	Linear distance between adjacent panel centers within a given panel strip in the direction of increasing or decreasing panel index depending on the subscript
i	Panel index
j	Panel index
K	Number of blades
k	Blade number 1, 2,... K
L	Number of streamwise wake panels
l	Index of streamwise wake panels
m	panel index
N	Number of panels on each propeller blade and the associated portion of the hub
N_C	Number of blade panels in the chordwise direction (streamwise for sphere)

N_S	Number of blade panels in the spanwise direction (circumferential for sphere)
$P - xr\theta$	Propeller cylindrical coordinate system
$P - xyz$	Propeller cartesian coordinate system
P_I	Pressure at the propeller center
$Pn - cs$	Panel coordinate system
$Pn - op$	Panel Cartesian coordinate system
Q_W	Point on wake surface
R	Propeller radius
r	Radial distance from center of sphere
r	Radial distance from x-axis in $P - xr\theta$
r'	non-dimensional propeller radius
R_H	Propeller hub radius
R_{sphere}	Sphere radius
S	Combined blade, hub, and wake surfaces
s_1	Panel geometry parameter used in Equations (3.14) & (3.15)
s_2	Panel geometry parameter used in Equations (3.14) & (3.15)
s_3	Panel geometry parameter used in Equations (3.14) & (3.15)
S_B	Propeller blade surface
S_H	Propeller hub surface
S_j	Surface area of panel j
S_W	Propeller wake surface
$SLAE_1$	First system of linear algebraic equations
$SLAE_2$	Second system of linear algebraic equations
u	Spanwise panel index (circumferential for sphere)
U_∞	Velocity at infinity

v	Chordwise panel index (streamwise for sphere)
v_c	Perturbation velocity in the panel chordwise direction
v_o	Perturbation velocity in the panel o direction
v_p	Perturbation velocity in the panel p direction
v_s	Perturbation velocity in the panel spanwise direction
$V_{\pm j}$	Velocity magnitude at the center of the suction(+) or pressure(-) side trailing edge panels of the jth spanwise strip
$W_{ij^{TE}}$	Influencing potential on panel i from doublet distribution on wake panel(s) j
x	Distance along the x-axis in $P-xyz$ and $P-xr\theta$
y	Distance along the y-axis in $P-xyz$
z	Distance along the z-axis in $P-xyz$

Abstract

This report describes the governing equation and boundary conditions for a marine propeller operating in a uniform flow field of inviscid and irrotational fluid. A method is presented by which the velocity and pressure on the blade surface of the propeller can be numerically simulated, using hyperboloidal, constant strength source and doublet panels. Accuracy of the numerical method is verified through comparison with analytically known results and the ability of the numerical simulation to predict the thrust and torque on a propeller in open water is assessed through comparison with published experimental results. The thrust and torque results for the propeller are near the experimental measurements but do not converge to a common value as the panel size decreases.

Keywords: Propeller, Marine, Hyperboloidal, Panel, Source, Doublet, Inviscid, Open-water, Thrust, Torque,

1 Introduction

The design of a ship's propeller can be described as an optimization problem with the objective of maximizing efficiency, and constrained by the limitations of strength and often cavitation. Systematic series have long been used to size propellers in early phase ship design, however their applicability is limited to the range of sizes and shapes which constitute the series, precluding the use of systematic series in the design of new and novel propeller concepts. Various classes of numerical methods exist for solving the flow around a propeller, each with their own set of advantages and disadvantages. Lifting surface methods have been shown to predict thrust and torque with a reasonable degree of accuracy [8]. Lifting surface methods however, do not model the thickness of the blade and thus cannot be used to analyze the effect of blade section shape on thrust, torque, or cavitation. This inability to evaluate the effects of different blade section shapes leaves lifting surface methods unable to the evaluate the effects of structural constraints, which manifest themselves as constraints on blade section thickness. Finite volume or other methods used to solve the Navier-Stokes equations have the ability to accurately predict the hydrodynamic quantities needed in the design of a marine propeller and can evaluate the effects of different blade section shapes [12]. However, resource limitations preclude their use in an optimization routine which will require frequent and numerous evaluations of different geometry and boundary conditions. Boundary element methods which solve the Laplace equation for the inviscid and irrotational flow around the true geometry of the propeller blade, have the ability to evaluate differences in blade section shape and the computational resources needed to execute the method can be met by the average personal computer. This report will discuss one such boundary element method, adapted from Hoshino [2], and evaluate its ability to predict the hydrodynamic quantities needed in a propeller design. It is the hope of the author that this method may be later used as a hydrodynamic analysis tool in the optimization of a marine propeller, where the hydrodynamic and structural properties of the blade are simultaneously evaluated.

2 The Propeller Flow Problem

2.1 Propeller Geometry and Coordinate System

We define the propeller Cartesian coordinate system $P{-}xyz$ such that the x-axis is concentric with the shaft axis and positive downstream, the z-axis extends upward from the shaft centerline bisecting the nose-tail line of a blade section at the propeller hub, and the y-axis is such that we have a right handed coordinate system. It will be convenient to define a cylindrical propeller coordinate system $P - xr\theta$ such that the x-axis is the same as that of $P - xyz$ but where r is the radial distance from the x-axis and θ increases moving clockwise from the z-axis, looking downstream. The cylindrical coordinate system can be transformed into the Cartesian system $P - xyz$ using the following relations:

$$x = x \tag{2.1}$$

$$y = -r\sin\theta \tag{2.2}$$

$$z = r\cos\theta \tag{2.3}$$

The midchord line at any radius can be located using the following relations:

$$\mathbf{MC}(r', k) = \begin{bmatrix} MC_x \\ MC_y \\ MC_z \end{bmatrix} = \begin{bmatrix} \chi(r') \\ -r\sin\big(\xi(r') + \theta_k(k)\big) \\ r\cos\big(\xi(r') + \theta_k(k)\big) \end{bmatrix} \tag{2.4}$$

where:

$r' = \frac{r - R_H}{R - R_H}$

R is the propeller radius

R_H is the propeller hub radius

$\theta_k(k)$ is the angular location of the blade midchord at the hub of blade k, with respect to the z-axis

k is the blade number 1, 2,..., K

K is the number of blades

$\chi(r')$ is the blade rake as a function of r'

$\xi(r')$ is the blade skew as a function of r'

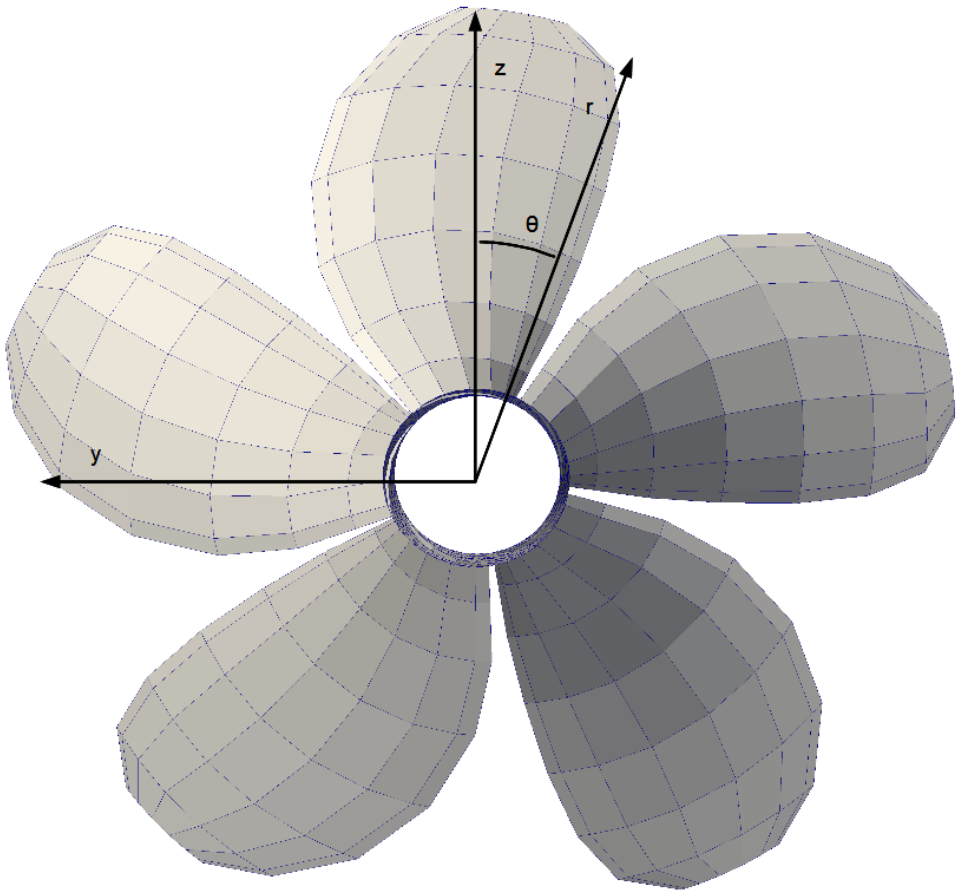

Figure 2.1: Propeller Cartesian and cylindrical coordinate systems (looking downstream)

The nose-tail line can be located using the following relationship:

$$\mathbf{NT}(r',k,e) = \begin{bmatrix} NT_x \\ NT_y \\ NT_z \end{bmatrix} = \begin{bmatrix} \chi(r') + \left(eC(r') - \frac{C(r')}{2}\right)\sin\gamma(r') \\ -r\sin\left(\xi(r') + \theta_k(k) + \left(\frac{eC(r')}{r} - \frac{C(r')}{2r}\right)\cos\gamma(r')\right) \\ r\cos\left(\xi(r') + \theta_k(k) + \left(\frac{eC(r')}{r} - \frac{C(r')}{2r}\right)\cos\gamma(r')\right) \end{bmatrix} \tag{2.5}$$

where:

- $C(r')$ is the blade chord length as a function of r'
- e is the non-dimensional, unit chord, such that 0 is the leading edge and 1 is the trailing edge
- $\gamma(r')$ is the blade pitch angle as a function of r'

It should be noted that for a propeller the chord $C(r')$ is the length between a leading edge point and a trailing edge point along a plane of constant radius, thus C is the length of an arc measured along a helix. Also, here the blade pitch angle γ is the geometric pitch angle measured along the nose-tail line of the blade section.

The blade section shape at any radius can be described by a half-thickness shape function $\tau(\tau_{max}, e)$ and a camber shape function $\epsilon(\epsilon_{max}, e_{max}, e)$, where:

- τ_{max} is the maximum thickness of the section and is a function of r'
- ϵ_{max} is the maximum camber of the section and is a function of r'
- e_{max} is the location where the maximum camber thickness occurs along the nose-tail line and is also a function of r'

These section shape functions are analogous to those used to describe foil section series, like the NACA series. Using them we can locate the blade surface with the following equations:

$$\mathbf{BS}(r',e,k) = \begin{bmatrix} NT_x(r',e,k) - \tau\sin\alpha\sin\gamma - \epsilon\cos\gamma - \tau\cos\alpha\cos\gamma \\ -r\sin\left(\xi + \theta_k + \left(\frac{eC}{r} - \frac{C}{2r}\right)\cos\gamma - \frac{\tau\sin\alpha}{r}\cos\gamma + \frac{\epsilon}{r}\sin\gamma + \frac{\tau\cos\alpha}{r}\sin\gamma\right) \\ r\cos\left(\xi + \theta_k + \left(\frac{eC}{r} - \frac{C}{2r}\right)\cos\gamma - \frac{\tau\sin\alpha}{r}\cos\gamma + \frac{\epsilon}{r}\sin\gamma + \frac{\tau\cos\alpha}{r}\sin\gamma\right) \end{bmatrix} \tag{2.6}$$

$$\mathbf{BP}(r',e,k) = \begin{bmatrix} NT_x(r',e,k) - \tau\sin\alpha\sin\gamma - \epsilon\cos\gamma + \tau\cos\alpha\cos\gamma \\ -r\sin\left(\xi + \theta_k + \left(\frac{eC}{r} - \frac{C}{2r}\right)\cos\gamma + \frac{\tau\sin\alpha}{r}\cos\gamma + \frac{\epsilon}{r}\sin\gamma - \frac{\tau\cos\alpha}{r}\sin\gamma\right) \\ r\cos\left(\xi + \theta_k + \left(\frac{eC}{r} - \frac{C}{2r}\right)\cos\gamma + \frac{\tau\sin\alpha}{r}\cos\gamma + \frac{\epsilon}{r}\sin\gamma - \frac{\tau\cos\alpha}{r}\sin\gamma\right) \end{bmatrix} \tag{2.7}$$

where **BS** and **BP** are vectors to the blade surface on the suction and pressure sides respectively. Equations (2.6) and (2.7) will be used later in discretizing the blade surface.

2.2 Velocity Potential and Boundary Conditions

The flow field in which the propeller operates can be described by the linear combination of a free-stream velocity potential and a perturbation velocity potential ϕ which both satisfy the Laplace Equation.

$$\nabla^2\phi = 0$$

The perturbation potential also must become zero at an infinite distance away from the propeller.

Consider a boundary surface S which consists of a propeller blade surface S_B, a hub surface S_H and a wake surface S_W with normal vector $\mathbf{n}$ pointing into the fluid domain. Applying Green's identity, the perturbation velocity potential ϕ at any field point $\mathbf{P}(x, y, z)$ can be found from a distribution of sources and doublets on the surface S. The relationship for ϕ can be written as follows [2]:

$$4\pi E\phi(\mathbf{P}) = \iint_S \phi(\mathbf{Q})\frac{\partial}{\partial \mathbf{n_Q}}\left(\frac{1}{R(\mathbf{P},\mathbf{Q})}\right)dS - \iint_S \frac{\partial\phi(\mathbf{Q})}{\partial \mathbf{n_Q}} \cdot \frac{1}{\mathbf{R}(\mathbf{P},\mathbf{Q})}dS \tag{2.8}$$

where

$$E = \begin{cases} 0 & \text{for the point } \mathbf{P} \text{ inside S,(not in the fluid domain)} \\ 1/2 & \text{for the point } \mathbf{P} \text{ on S,} \\ 1 & \text{for the point } \mathbf{P} \text{ outside S,(in the fluid domain)} \end{cases}$$

$\mathbf{Q}$ is a vector locating a point on the surface S
$\mathbf{n_Q}$ is the normal vector at point $\mathbf{Q}$ pointing into the fluid domain
$\mathbf{R} = \mathbf{Q} - \mathbf{P}$
$\frac{\partial}{\partial \mathbf{n_Q}}$ is the normal derivative at $\mathbf{Q}$

The solution of equation (2.8) is made unique through the application of a kinematic boundary condition, imposed on S_B and S_H such that the normal velocity on those surfaces is zero. This can be expressed through equation (2.9).

$$\frac{\partial\phi(\mathbf{Q})}{\partial \mathbf{n_Q}} = -\mathbf{V_I} \cdot \mathbf{n_Q} = -(\mathbf{V_{inf}} + \mathbf{\Omega} \times \mathbf{Q}) \cdot \mathbf{n_Q} \tag{2.9}$$

where $\mathbf{V_{inf}}$ is the free stream velocity, $\mathbf{\Omega}$ is the rotational speed of the propeller, and $\mathbf{V_I}$ is the resultant incident velocity on the propeller blade surface. Imposing the kinematic boundary condition in (2.9), the second term on the right hand side of equation (2.8) can be satisfied using a constant source distribution on surfaces S_B and S_H.

We assume that there is no flow through nor a pressure jump across the wake surface S_W, however a discontinuity of the potential $\Delta\phi$ is allowed. For the steady problem, $\Delta\phi$ is constant along any stream line in the wake and can be written as

$$\Delta\phi = \phi_+ - \phi_- \tag{2.10}$$

where ϕ_+ is the potential on the suction side of the wake and ϕ_- the potential on the pressure side.

Applying the kinematic boundary condition via equation (2.9) and the wake boundary condition via equation (2.10) to equation (2.8) we get equation (2.11) as per Hoshino [2].

$$2\pi E\phi(\mathbf{P}) - \iint_{S_B+S_H} \phi(\mathbf{Q}) \frac{\partial}{\partial \mathbf{n_Q}} \left(\frac{1}{\mathbf{R}(\mathbf{P},\mathbf{Q})} \right) dS - \iint_{S_W} \Delta\phi(\mathbf{Q_W}) \frac{\partial}{\partial \mathbf{n_{Q_W}}} \left(\frac{1}{\mathbf{R}(\mathbf{P},\mathbf{Q})} \right) dS = \iint_{S_B+S_H} (\mathbf{V_I} \cdot \mathbf{n_Q}) \frac{1}{\mathbf{R}(\mathbf{P},\mathbf{Q})} dS \quad (2.11)$$

Here Q_W indicates a point on the wake surface. Integrals over S_B and S_H are Cauchy principal value integrals. Equation (2.11) can be solved uniquely for ϕ, and the resulting potential distribution can be differentiated to obtain velocities. However, we are not yet assured that the Kutta condition is satisfied. Hess [1] states that the Kutta condition can be applied numerically in 3D by making the surface pressures (or velocity magnitude in the case of potential flow) on the suction and pressure side surfaces have a common limit as the trailing edge is approached. It is by these means that the Kutta condition will be satisfied in this work. Satisfaction of the Kutta condition will be discussed in more detail in the next chapter.

3 Discretization and Numerical Method

Figure 3.1 illustrates the process used to numerically solve the propeller flow problem satisfying the Kutta condition. The important steps of this process will be detailed in this chapter.

3.1 Discretization of the Blade, Hub, and Wake Surfaces

The blade, hub, and wake surfaces will be discretized into a number of quadrilateral panels. The panel shape and any point on the panel surface is described by Morino [10] via equations (3.1) and (3.2), creating a hyberboloidal quadrilateral panel.

$$\mathbf{Q} = \mathbf{q}_0 + \zeta\mathbf{q}_1 + \eta\mathbf{q}_2 + \zeta\eta\mathbf{q}_3 \tag{3.1}$$

$$\begin{bmatrix} \mathbf{q}_0 \\ \mathbf{q}_1 \\ \mathbf{q}_2 \\ \mathbf{q}_3 \end{bmatrix} = \frac{1}{4}\begin{bmatrix} 1 & 1 & 1 & 1 \\ 1 & 1 & -1 & -1 \\ 1 & -1 & 1 & -1 \\ 1 & -1 & -1 & 1 \end{bmatrix}\begin{bmatrix} \mathbf{q}_{++} \\ \mathbf{q}_{+-} \\ \mathbf{q}_{-+} \\ \mathbf{q}_{--} \end{bmatrix} \tag{3.2}$$

Here $\mathbf{q}_{++}$, $\mathbf{q}_{+-}$, $\mathbf{q}_{-+}$, and $\mathbf{q}_{--}$ are corner points of a panel and ζ and η are local parametric variables with the domain $\zeta, \eta \in [-1, 1]$. Figure 3.2 illustrates a typical panel and figure 3.3 shows an example of a discretized blade, the hub surface between it and an adjacent blade, and the associated wake surface. It is important to note that these panels are not planar and that their bounding edges may be twisted, allowing all panel corners to lay on the blade surface, increasing the accuracy in which the blade is modeled.

Using equations (2.6) and (2.7) to find the panel corners we can discretize the propeller hub and blades through systematic variations of r' and e. The blade will be divided into N_S panels spanwise and N_C panels chordwise on each side of the blade, giving $2N_SN_C$ panels per blade. We will use a cosine spacing in the spanwise direction and a uniform spacing in the chordwise direction such that

$$r' = 1/2 - \frac{1}{2}\cos f \tag{3.3}$$

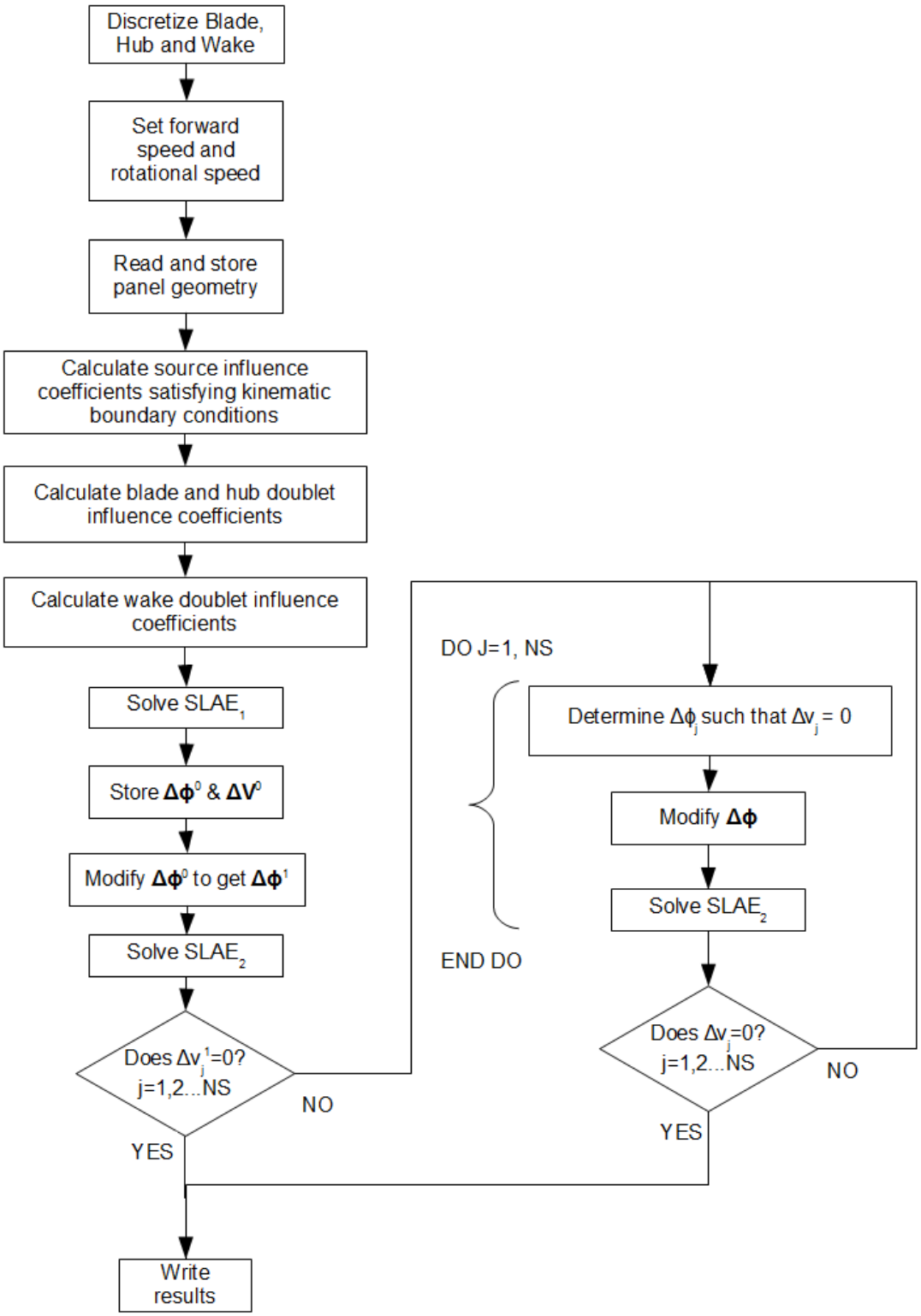

Figure 3.1: Flow chart of numerical solution method

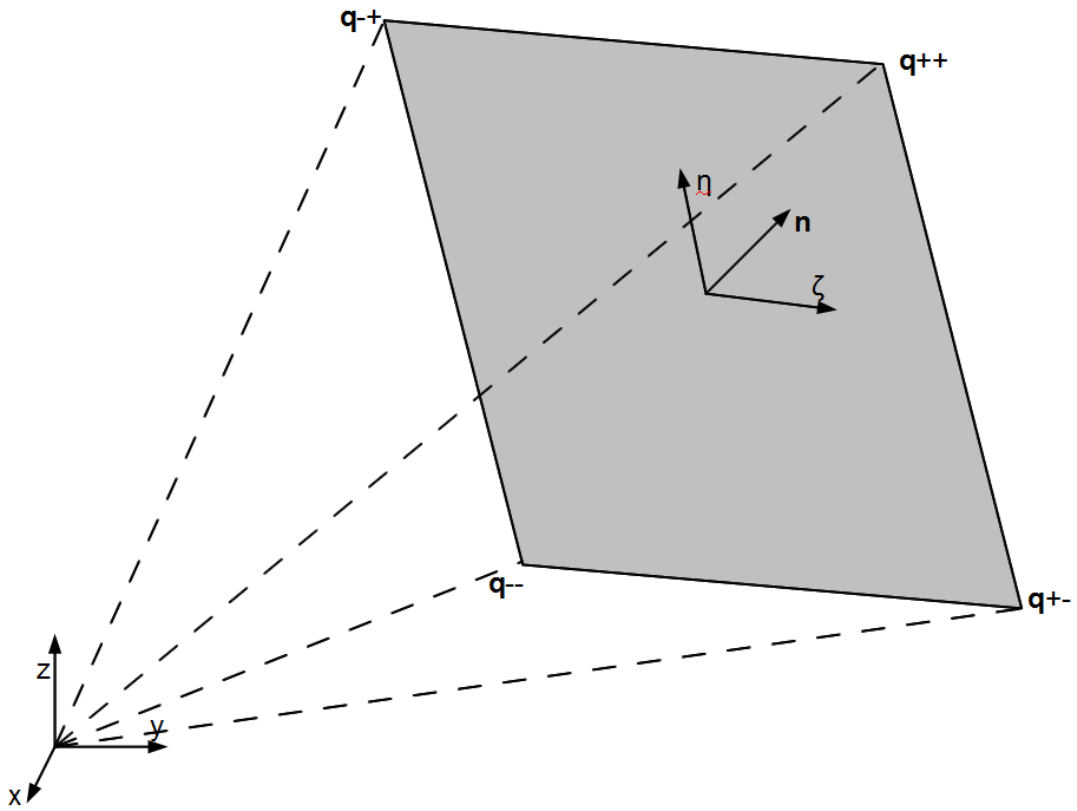

Figure 3.2: Hyperboloidal quadrilateral panel

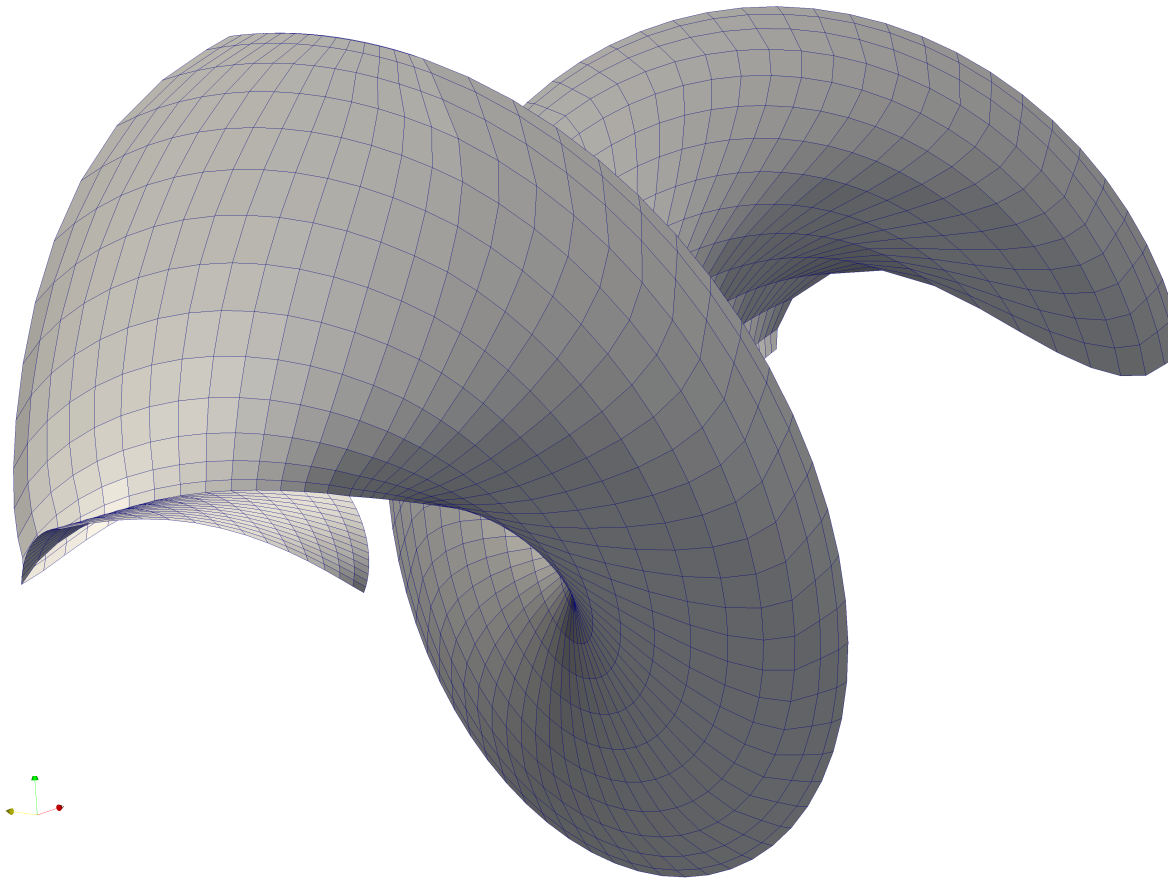

Figure 3.3: Panels on the blade, hub, and wake for the key blade

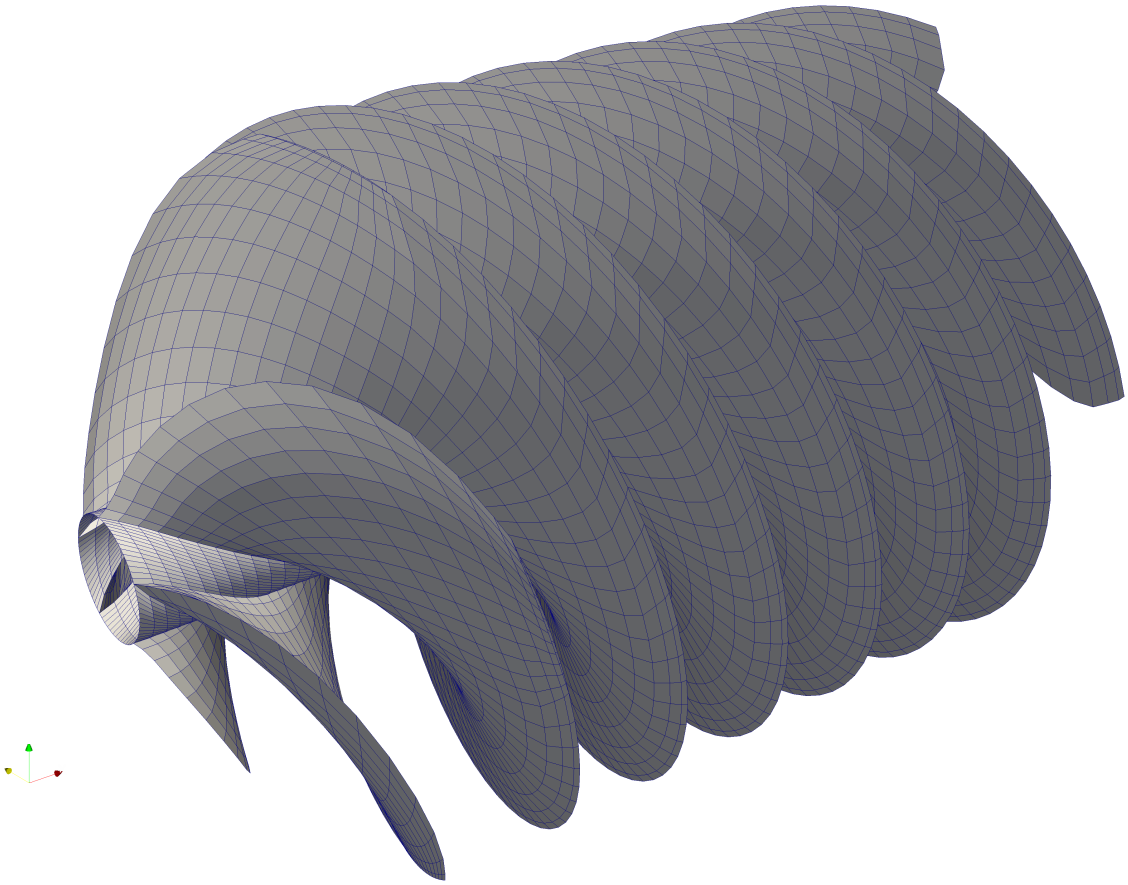

Figure 3.4: Panels on the blade, hub, and wake for the propeller

where

$$f = \begin{cases} 0 & \text{for } u = 1 \\ \dfrac{(2u-1)\pi}{2(N_S+1)} & \text{for } u = 2,\, 3,\ldots,\, N_S+1 \end{cases}$$

and

$$e = \frac{v}{N_C} \tag{3.4}$$

where $v = 0,\, 1,\, \ldots,\, N_C$.

The hub surface has been discretized in the chordwise direction using the same uniform spacing that is used discretize the root section of the blade. The corner points of the hub panels lay on helical arcs which connect the corners of the blade root panels on the suction side of one blade to the corners of blade root panels on the pressure side of the adjacent blade. These helical arcs are uniformly divided into N_S panels, creating $N_S N_C$ panels on the hub section between each blade. An example of the hub panels can be seen in figure 3.3.

The blade wake has been approximated by strips of constant strength doublet panels emanating from the pairs of trailing edge panels on the blade surface. These panels continue downstream from the trailing edge with a constant pitch equal to the geometric pitch γ of the blade at that radius. Each wake panel represents a $\frac{4}{3N_S}$ radian angular displacement around the helix of that wake strip, thus the panel size on a given radial wake strip is constant along the helix of the that wake strip. Each wake strip consists of L panels.

3.2 First System of Linear Algebraic Equations

Having divided the blade and hub surfaces S_B and S_H into $K \times N$ panels we can write equation (2.11) as a system of N linear algebraic equations. Here N is the number of panels on the key blade and its surrounding hub section. Due to the symmetry of the steady propeller problem we need only solve for the perturbation potential on one blade and its surrounding hub section, accounting for the influence of the other propeller surfaces on that key blade. ϕ_j and $\mathbf{V_I} \cdot \mathbf{n_Q}$ are assumed to be constant within each panel and equal to the value at the centroid of the panel. The first system of linear equations $SLAE_1$ then can be written as

$$\sum_{j=1}^{N} (\delta_{ij} - C_{ij})\, \phi_j = \sum_{j=1}^{N} B_{ij} (\mathbf{V_I} \cdot \mathbf{n_Q}) \tag{3.5}$$

$$\text{for } i = 1,\, 2,\, \ldots,\, N$$

The source and body doublet influence coefficients are written as B_{ij} and C_{ij} respectively. In equation (3.5), the i index refers to the row of the system matrix and the point being affected by the influence coefficient. The j index indicates the influencing panel and the column in the left hand side matrix. The source and body doublet influence coefficients, B_{ij} and C_{ij}, include the influence from sister panels on all blades onto the collocation point on the key blade. Equations for the calculation of the influence coefficients are provided later in this chapter which mathematically describe the process by which the influence from each

blade is included. In equation (3.5) δ is the Kronecker delta.

$SLAE_1$ is merely solved as the initial condition in the iterative method used to satisfy the Kutta condition. The solution of $SLAE_1$ does not include the influence of the wake nor does it satisfy the Kutta condition.

After solving $SLAE_1$ we will calculate and store two vectors $\mathbf{\Delta}\phi$ and $\mathbf{\Delta V}$, both with dimension N_S, to be used in the iterative satisfaction of the Kutta condition.

$$\mathbf{\Delta}\phi = \begin{bmatrix} \Delta\phi_1 \\ \Delta\phi_2 \\ \vdots \\ \Delta\phi_{N_S} \end{bmatrix} = \begin{bmatrix} \phi_{+1^{TE}} - \phi_{-1^{TE}} \\ \phi_{+2^{TE}} - \phi_{-2^{TE}} \\ \vdots \\ \phi_{+N_S^{TE}} - \phi_{-N_S^{TE}} \end{bmatrix}$$

$$\mathbf{\Delta V} = \begin{bmatrix} \Delta V_1 \\ \Delta V_2 \\ \vdots \\ \Delta V_{N_S} \end{bmatrix} = \begin{bmatrix} V_{+1^{TE}} - V_{-1^{TE}} \\ V_{+2^{TE}} - V_{-2^{TE}} \\ \vdots \\ V_{+N_S^{TE}} - V_{-N_S^{TE}} \end{bmatrix}$$

Where $\phi_{\pm j^{TE}}$ and $V_{\pm j^{TE}}$ are the perturbation potential and velocity magnitude at the center of the suction(+) or pressure(-) side trailing edge panels of the jth spanwise strip. The TE subscript indicates that the value appears only when panel j is a trailing edge panel.

3.3 Second System of Linear Algebraic Equations

In our second system of linear algebraic equations $SLAE_2$, we have included the influence of the wake $W_{ij^{TE}}$ on the right hand side of the system and will specify values of $\Delta\phi_{j^{TE}}$ attempting to satisfy the Kutta condition. Here again the TE subscript indicates that the wake influence is only added when panel j is a trailing edge panel. The manner in which values of $\Delta\phi_{j^{TE}}$ are chosen is discussed later in this chapter.

$$\sum_{j=1}^{N} (\delta - C_{ij})\, \phi_j = \sum_{j=1}^{N} \left[B_{ij}(\mathbf{V_I} \cdot \mathbf{n_Q}) + W_{ij^{TE}} \Delta\phi_{j^{TE}} \right] \tag{3.6}$$

$$\text{for } i = 1,\, 2,\, \ldots,\, N$$

The wake influence coefficient $W_{ij^{TE}}$ is the influence of an entire streamwise wake strip consisting of L panels and the influence of sister wake strips from other blades, onto a collocation point on the key blade. The equations used to calculate the wake influence coefficient are given in the next section.

3.4 Influence Coefficients

The influence coefficients used in equations (3.5) and (3.6) and the manner in which effects from the other blades have been taken into account is show below. We see that the influence of multiple blades is conglomerated into a single coefficient. The influence of each wake panel in a streamwise strip is accounted for in the same manner.

$$C_{ij} = \sum_{k=1}^{K} \left[\frac{1}{2\pi} \iint_{S_j} \frac{\partial}{\partial \mathbf{n_j}} \left(\frac{1}{\mathbf{R_{ijk}}} \right) dS_j \right] \tag{3.7}$$

$$W_{ij} = \sum_{k=1}^{K} \sum_{l=1}^{L} \left[\frac{1}{2\pi} \iint_{S_j} \frac{\partial}{\partial \mathbf{n_j}} \left(\frac{1}{\mathbf{R_{ijk}}} \right) dS_j \right] \tag{3.8}$$

$$B_{ij} = \sum_{k=1}^{K} \left[-\frac{1}{2\pi} \iint_{S_j} \left(\frac{1}{\mathbf{R_{ijk}}} \right) dS_j \right] \tag{3.9}$$

$\mathbf{R_{ijk}}$ is here defined as

$$\mathbf{R_{ijk}} = \mathbf{Q_{jk}}(\zeta, \eta) - \mathbf{P_i} \tag{3.10}$$

We also define;

$$\mathbf{s_1}(\zeta, \eta) = \frac{\partial \mathbf{Q}(\zeta, \eta)}{\partial \zeta} \tag{3.11}$$

$$\mathbf{s_2}(\zeta, \eta) = \frac{\partial \mathbf{Q}(\zeta, \eta)}{\partial \eta} \tag{3.12}$$

$$\mathbf{s_3}(\zeta, \eta) = \frac{\mathbf{s_1} \times \mathbf{s_2}}{|\mathbf{s_1} \times \mathbf{s_2}|} \tag{3.13}$$

Using the terms $\mathbf{R}$, $\mathbf{s_1}$, $\mathbf{s_2}$, and $\mathbf{s_3}$ we define the following as per Hsin [4].

$$I_D(\zeta, \eta) = \frac{1}{2\pi} \tan^{-1} \left(\frac{(\mathbf{R} \times \mathbf{s_1}) \cdot (\mathbf{R} \times \mathbf{s_2})}{|\mathbf{R}||\mathbf{R} \cdot (\mathbf{s_1} \times \mathbf{s_2})|} \right) \tag{3.14}$$

$$I_S(\zeta, \eta) = -\frac{1}{2\pi} \left\{ -\frac{(\mathbf{R} \times \mathbf{s_1}) \cdot \mathbf{s_3}(0,0)}{|\mathbf{s_1}|} \sinh^{-1} \left(\frac{\mathbf{R} \cdot \mathbf{s_1}}{|\mathbf{R} \times \mathbf{s_1}|} \right) + \frac{(\mathbf{R} \times \mathbf{s_2}) \cdot \mathbf{s_3}(0,0)}{|\mathbf{s_2}|} \sinh^{-1} \left(\frac{\mathbf{R} \cdot \mathbf{s_2}}{|\mathbf{R} \times \mathbf{s_2}|} \right) \right\} \tag{3.15}$$

and

$$\epsilon(\zeta, \eta) = \frac{\mathbf{R} \cdot (\mathbf{s_1} \times \mathbf{s_2}}{|\mathbf{R} \cdot (\mathbf{s_1} \times \mathbf{s_2}|} \tag{3.16}$$

Using equations (3.14) - (3.16), we can evaluate the integrals in our influence coefficients

such that,

$$\Phi_D = \frac{1}{2\pi}\iint_{S_j} \frac{\partial}{\partial \mathbf{n_j}}\left(\frac{1}{\mathbf{R_{ijk}}}\right) dS_j$$
$$= \begin{cases} 0 & \text{If, } I_D(1,1) + I_D(1,-1) + I_D(-1,1) + I_D(-1,-1) = 1 \\ \varphi_D - \frac{1}{2}\frac{\varphi_D}{|\varphi_D|} & \text{If, } \epsilon(1,1)\epsilon(1,-1)\epsilon(-1,1)\epsilon(-1,-1) < 0 \\ \varphi_D & \text{Else} \end{cases} \quad (3.17)$$

where

$$\varphi_D \;=\; \epsilon(1,1)I_D(1,1) \;-\; \epsilon(1,-1)I_D(1,-1) \;-\; \epsilon(-1,1)I_D(-1,1) \;+\; \epsilon(-1,-1)I_D(-1,-1) \quad (3.18)$$

and

$$-\frac{1}{2\pi}\iint_{S_j}\left(\frac{1}{\mathbf{R_{ijk}}}\right) dS_j = I_S(1,1) - I_S(1,-1) - I_S(-1,1) + I_S(-1,-1)$$
$$+ \left(\mathbf{R}(0,0)\cdot\mathbf{s_3}(0,0)\right)\Phi_D \quad (3.19)$$

3.5 Satisfaction of the Kutta Condition

The iterative process through which the Kutta condition is satisfied is illustrated in figure 3.1 and we will refer to that illustration in this description of the process. The Kutta condition must be satisfied at every spanwise set of trailing edge panels and to accomplish this we will choose a vector $\mathbf{\Delta}\phi$ such that every term of vector $\mathbf{\Delta V}$ is zero.

As illustrated in figure 3.1, once $SLAE_1$ is solved, the initial vectors $\mathbf{\Delta}\phi$ and $\mathbf{\Delta V}$ are obtained from the solution. We will identify this set of potential and velocity vectors by the superscript 0. Arbitrarily modifying $\mathbf{\Delta}\phi^0$, we create a new vector $\mathbf{\Delta}\phi^1$, the terms of which will be used to compute the wake influence in $SLAE_2$. Solving $SLAE_2$ with the wake influence scaled by $\mathbf{\Delta}\phi^1$, we obtain another set of velocity differentials at the trailing edge $\mathbf{\Delta V}^1$.

If every component of $\mathbf{\Delta V}^1$ does not vanish, we must estimate a new potential difference for each pair of trailing edge panels, $\Delta\phi_{newj^{TE}}$, which will make $\Delta V_{j^{TE}} = 0$ for that pair. Using our two sets of vectors $\mathbf{\Delta}\phi^0$, $\mathbf{\Delta V}^0$, $\mathbf{\Delta}\phi^1$, and $\mathbf{\Delta V}^1$, we can linearly model the relationship between $\Delta\phi_{j^{TE}}$ and $\Delta V_{j^{TE}}$ at each spanwise set of trailing edge panels and solve for the potential difference $\Delta\phi_{j^{TE}}$ which will make $\Delta V_{j^{TE}} = 0$. $\Delta\phi_{j^{TE}}$ is calculated and $SLAE_2$ is solved for each spanwise set of trailing edge panels individually. After $SLAE_2$ has been solved for every spanwise pair of trailing edge panels, the vector $\mathbf{\Delta V}$ is checked to see if every component is sufficiently close to zero.

If a term of $\mathbf{\Delta V}$ is not sufficiently close to zero, the set of vectors used to compute the relationship between $\Delta\phi_{j^{TE}}$ and $\Delta V_{j^{TE}}$ is updated, and the process is repeated.

3.6 Calculation of Velocity and Pressure on the Blade Surface

The velocities on the blade surfaces are obtained through numerical differentiation. This differentiation is done with respect to the local panel coordinate system, the perturbation velocity is combined with the free stream velocity, and the resultant converted to the propeller Cartesian coordinate system.

The perturbation potential field on the blade surface is modeled as two quadratic polynomials, $\phi_c(g)$ and $\phi_s(g)$, in the chordwise and spanwise directions respectively. Here g is the distance along the blade surface in either the chordwise or spanwise direction. The coefficients of the quadratic function are obtained from the solution of equation (3.20) for a, b, and c.

$$\begin{bmatrix} 0 & 0 & 1 \\ g_+^2 & g_+ & 1 \\ g_-^2 & g_- & 1 \end{bmatrix} \begin{bmatrix} a \\ b \\ c \end{bmatrix} = \begin{bmatrix} \phi_m \\ \phi_{m+1} \\ \phi_{m-1} \end{bmatrix} \tag{3.20}$$

Here m is either the spanwise panel index u or the chordwise panel index v depending on the direction for which the quadratic function is being fit. ϕ_m is the perturbation potential at the center of the panel where the velocity is being computed, and $\phi_{m\pm1}$ indicates an adjacent panel with either an increasing or decreasing panel index. In equation (3.20) $g_\pm$ is the linear distance between adjacent panel centers within a given panel strip in the direction of increasing or decreasing panel index depending on the subscript. Figure 3.5 illustrates this curve fitting for a simple case.

For the calculation of the velocity on a panel at the edge of the blade, where there is only one adjacent panel per strip, the differentiation is shifted. In an example where there is no panel index less than m, the system of equations describing the potential polynomial is similar to equation (3.20), however the panel of decreasing index has been replaced by a panel of index two greater than the panel of interest; as seen in equation (3.20). This effectively shifts the domain of the quadratic equation in the direction of increasing panel index.

$$\begin{bmatrix} 0 & 0 & 1 \\ g_+^2 & g_+ & 1 \\ g_{++}^2 & g_{++} & 1 \end{bmatrix} \begin{bmatrix} a \\ b \\ c \end{bmatrix} = \begin{bmatrix} \phi_m \\ \phi_{m+1} \\ \phi_{m+2} \end{bmatrix} \tag{3.21}$$

Here g_{++} is the distance from the center of the panel of interest to panel $m+2$, and ϕ_{m+2} is the perturbation potential at panel $m+2$. The same shift can be done in the opposite direction for the case where there is no panel with index greater than the panel where the velocity is to be computed.

The derivatives of $\phi_c(g)$ and $\phi_s(g)$ with respect to g are the perturbation velocities in the chordwise and spanwise directions, v_c and v_s. v_c and v_s are assumed to act in the direction of $\mathbf{q_1}$ and $\mathbf{q_2}$ respectively. We create a panel coordinate system $Pn-cs$ with unit vectors $\mathbf{c}$ and $\mathbf{s}$ in the direction of $\mathbf{q_1}$ and $\mathbf{q_2}$ respectively. $\mathbf{c}$ and $\mathbf{s}$ are not always normal to each other and the velocities v_c and v_s will need to be projected onto a Cartesian panel coordinate

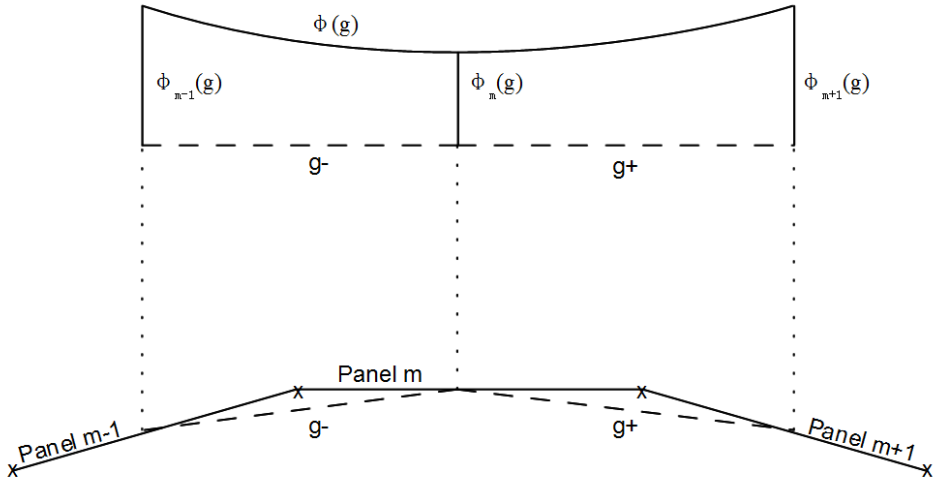

Figure 3.5: Sketch of method used in numerical differentiation of the perturbation potential

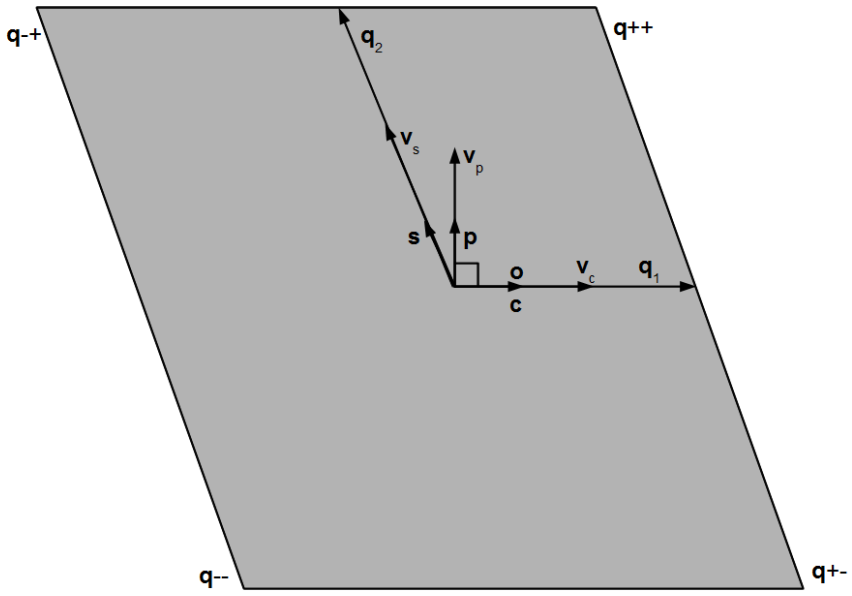

Figure 3.6: Local panel coordinate systems

system $Pn - op$ to be combined with the incident velocity $\mathbf{V_I}$. Coordinate systems $Pn - cs$ and $Pn - op$ are illustrated in figure 3.6. Figure 3.6 shows that $\mathbf{o} = \mathbf{c}$. The projection onto the $Pn - op$ coordinate system is accomplished through equations (3.22) and (3.23).

$$v_o = v_c \tag{3.22}$$

$$v_p = \frac{v_s - (\mathbf{s} \cdot \mathbf{o})v_c}{\mathbf{s} \cdot \mathbf{p}} \tag{3.23}$$

where:

- $\mathbf{s}$ is a unit vector in the direction of $\mathbf{q_2}$
- $\mathbf{o}$ is a unit vector of the $Pn - op$ Cartesian coordinate system described in the $P - xyz$ coordinate system
- $\mathbf{p}$ is a unit vector of the $Pn - op$ Cartesian coordinate system described in the $P - xyz$ coordinate system

Thus, the total velocity at the the panel center, in the panel Cartesian coordinate system is given by equation (3.24). The component normal to the panel surface is zero due to the application of the kinematic boundary condition on the blade surface.

$$\mathbf{V} = \begin{bmatrix} \mathbf{V_I} \cdot \mathbf{o} + v_o \\ \mathbf{V_I} \cdot \mathbf{p} + v_p \\ 0 \end{bmatrix} \tag{3.24}$$

The pressure on a panel is obtained using the Bernoulli equation such that

$$P = P_I + \frac{1}{2}\rho(|\mathbf{V_I}|^2 - |\mathbf{V}|^2) \tag{3.25}$$

where P_I is the reference pressure at the propeller center.

The pressure coefficient C_P follows as:

$$C_P = 1 - \frac{|\mathbf{V}|}{|\mathbf{V_I}|} \tag{3.26}$$

3.7 Calculation of Propeller Forces

The thrust F_x and the torque M_x acting on the propeller are obtained by integrating the pressure and viscous forces on the blade surfaces.

$$F_x = K \sum_{j=1}^{N} [P_j \Delta A_x + F_{\nu x}] \tag{3.27}$$

$$M_x = K \sum_{j=1}^{N} [(P_j \Delta A_z y - P_j \Delta A_y z) + (F_{\nu z} y - F_{\nu y} z)] \tag{3.28}$$

Where

P_j	is the pressure at panel j
$\mathbf{\Delta A}$	$= -\mathbf{n}\Delta A$, subscript indicates component direction
ΔA	is the panel area
$\mathbf{F}_\nu$	is the viscous force vector, subscript indicates component direction
y, z	panel center location in propeller Cartesian coordinate system $P - xyz$

The magnitude of the viscous force per panel is equal to

$$\frac{1}{2} \rho C_F \Delta A V^2 \tag{3.29}$$

where C_F is the ITTC friction coefficient [9] and V is the velocity magnitude on the panel. The viscous forces are assumed to act in the direction of the local velocity vector.

The advance ratio, thrust coefficient, torque coefficient and open-water efficiency are defined as

$$J = \frac{V_{Ix}}{nD} \tag{3.30}$$

$$K_T = \frac{F_x}{\rho n^2 D^4} \tag{3.31}$$

$$K_Q = \frac{M_x}{\rho n^2 D^5} \tag{3.32}$$

$$\eta_O = \frac{J}{2\pi} \frac{K_T}{K_Q} \tag{3.33}$$

4 Verification of the Method and Code

4.1 Sphere in Uniform Flow

Katz and Plotkin [5] describe the velocity potential field around a sphere in an otherwise uniform flow field as,

$$\Phi = U_\infty \cos\alpha \left(r + \frac{R_{sphere}^3}{2r^2} \right) \tag{4.1}$$

the resulting velocity field as,

$$\mathbf{V}_r = U_\infty \cos\alpha \left(1 - \frac{R_{sphere}^3}{r^3} \right) \tag{4.2}$$

$$\mathbf{V}_\alpha = -U_\infty \sin\alpha \left(1 + \frac{R_{sphere}^3}{2r^3} \right) \tag{4.3}$$

and the coefficient of pressure C_P on the sphere surface as

$$C_P = \left(1 - \frac{9}{4} \sin^2\alpha \right) \tag{4.4}$$

U_∞ is the free stream velocity, R_{sphere} is the radius of the sphere, r is the radial distance from the center of the sphere and α is the angle from the free-stream flow. In each of the equations above, the first term inside the parenthesis is the contribution from the free-stream and the second term represents the perturbation caused by the sphere.

To verify the accuracy of the method described in Chapter 3, a grid convergence study was performed using a sphere as the geometry, so that the results could be compared with equations (4.1) - (4.3). A sphere of unit radius was discretized using equations (4.5) - (4.7) to determine location of the panel corners in a Cartesian coordinate system with the origin at the center of the sphere.

$$x = -R_{sphere} \cos\left(\frac{v\pi}{N_C} \right) \tag{4.5}$$

$$y = \begin{cases} -0.001\cos(\frac{u\pi}{N_S}) & \text{If } v = 0 \text{ or } N_C, \\ -R_{sphere}\sin(\frac{v\pi}{N_C})\cos(\frac{u\pi}{N_S}) & \text{Else.} \end{cases} \tag{4.6}$$

$$z = \begin{cases} -0.001\sin(\frac{u\pi}{N_S}) & \text{If } v = 0 \text{ or } N_C, \\ -R_{sphere}\sin(\frac{v\pi}{N_C})\sin(\frac{u\pi}{N_S}) & \text{Else.} \end{cases} \tag{4.7}$$

Where

R_{sphere} = Radius of the sphere
N_C = number of streamwise panels on half of the sphere
N_S = number of circumferential panels on half of the sphere
u = 0, 1,. . . , N_S
v = 0, 1,. . . , N_C

The special case where v equals either zero or N_C has been implemented to insure that no panel corners are co-located, which causes one of the principal vectors used to compute the panel influence functions to become degenerate.

The other half of the sphere is paneled by mirroring the panel corners about the X-Y plane. The term $\frac{v\pi}{N_C}$ in equations (4.5) - (4.7) is equal to α in equations (4.1) - (4.3) thus panel centers are located at intervals of π/N_C streamwise around the sphere. Figure 4.1 illustrates the panel arrangement on a sphere where $N_C = N_S = 9$. No wake has been modeled for this problem as no lift is developed.

Figure 4.2 shows the difference between the perturbation potential from equation (4.1) and the numerical results at panels centers, plotted over half of the sphere. Results are given for cases where $N_C = N_S = 3, 9,$ & 27. From figure 4.2 one can see that the results converge rapidly to equation (4.1) as the number of panels is increased. Figures 4.3 and 4.4 show values of V_θ and C_P on a sphere of unit radius in a unit free stream flow. The maximum and minimum values that occur for the quantities shown are printed at the top and bottom of the color scale. The sphere in figures 4.3 and 4.4 has been paneled with parameters N_C and $N_S = 27$.

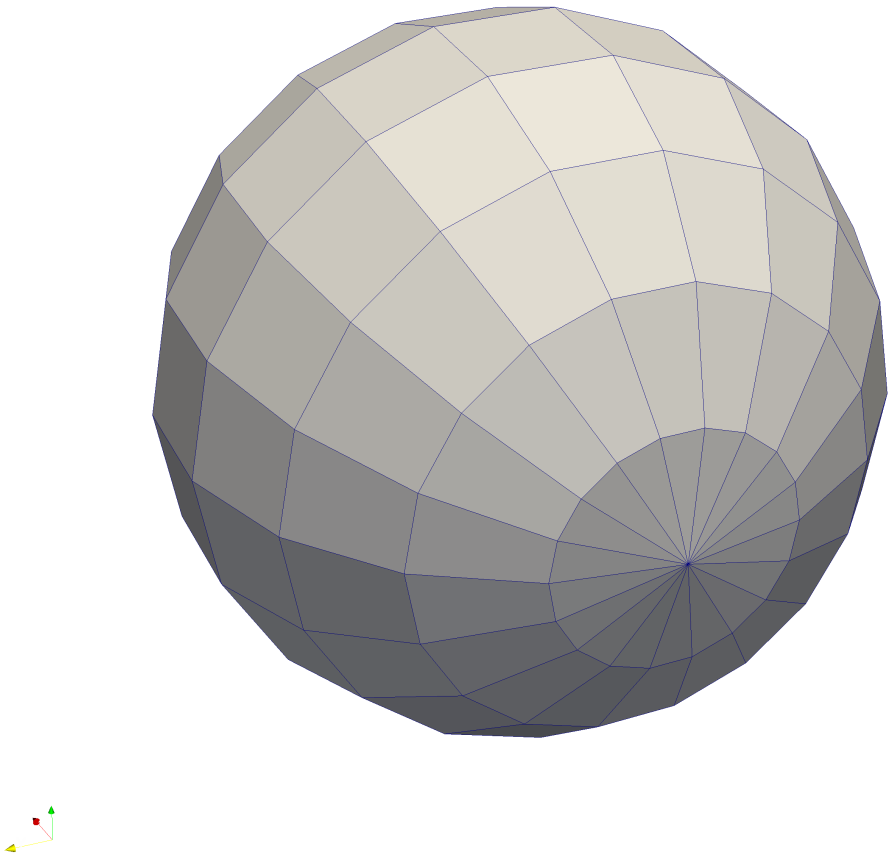

Figure 4.1: Panels on Surface of a Sphere, $N_C = N_S = 9$

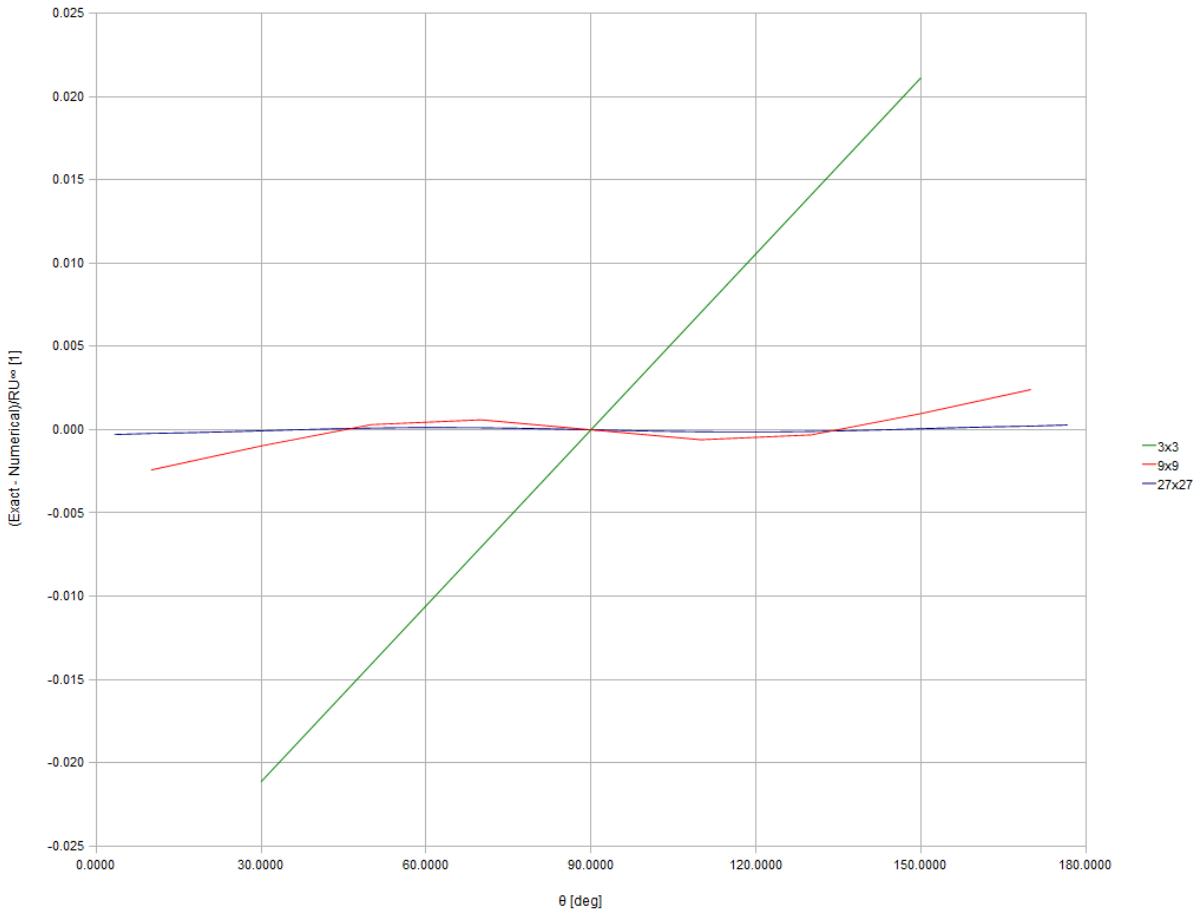

Figure 4.2: Difference between the exact velocity potential and the numerical value

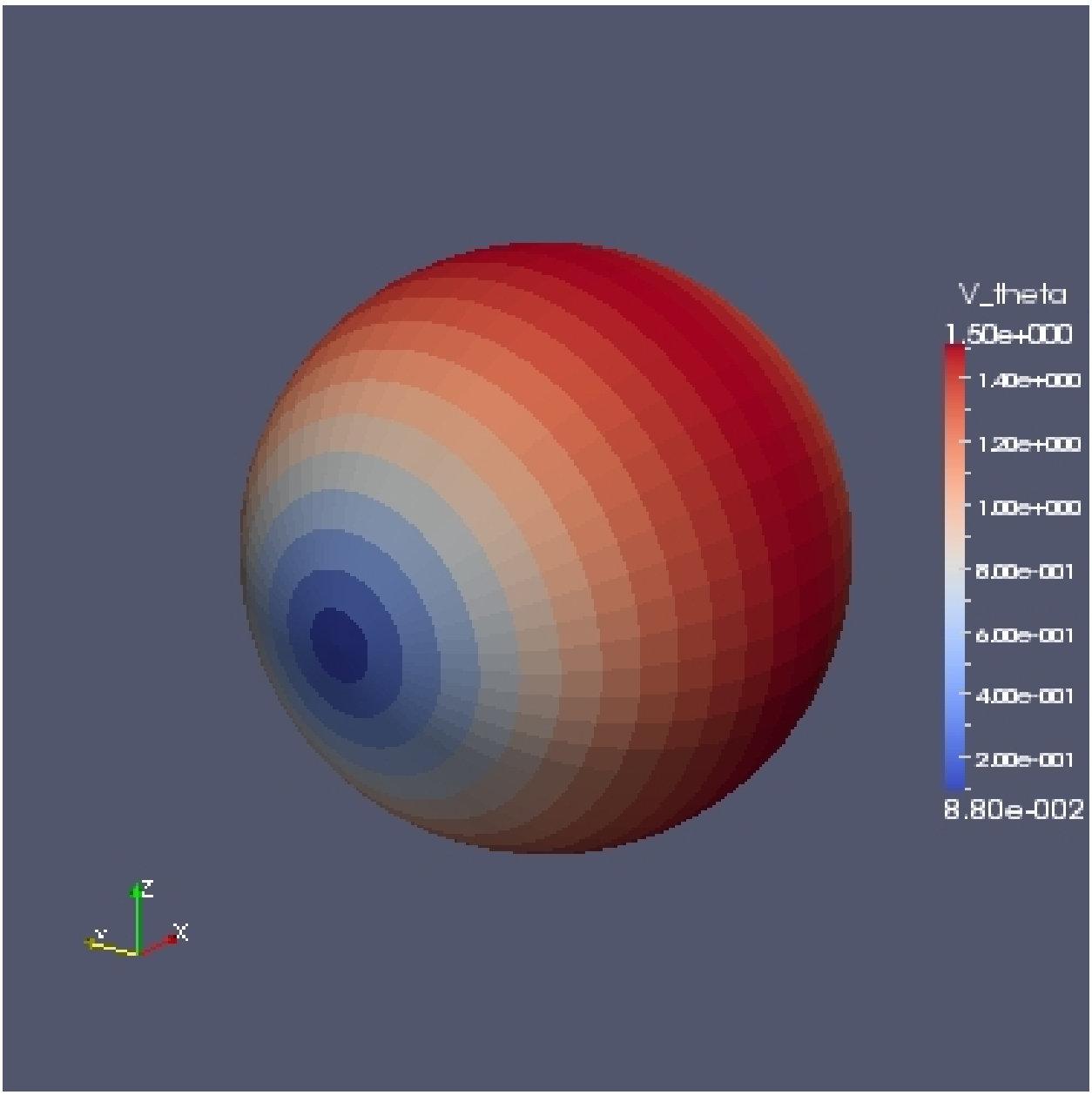

Figure 4.3: V_α on surface of sphere, $R_{sphere} = 1$, $U_\infty = 1$

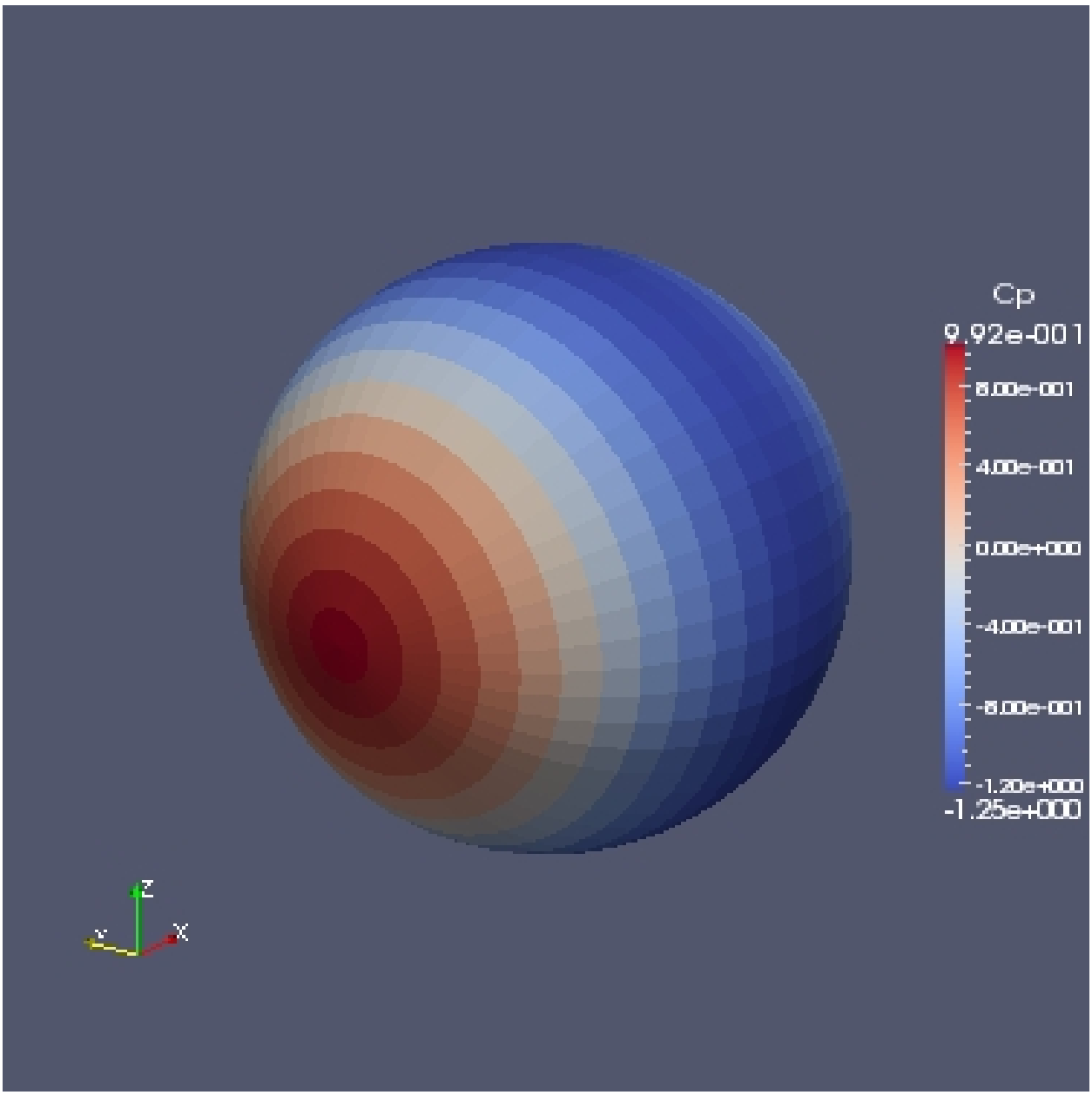

Figure 4.4: C_P on surface of sphere, $R_{sphere} = 1$, $U_\infty = 1$

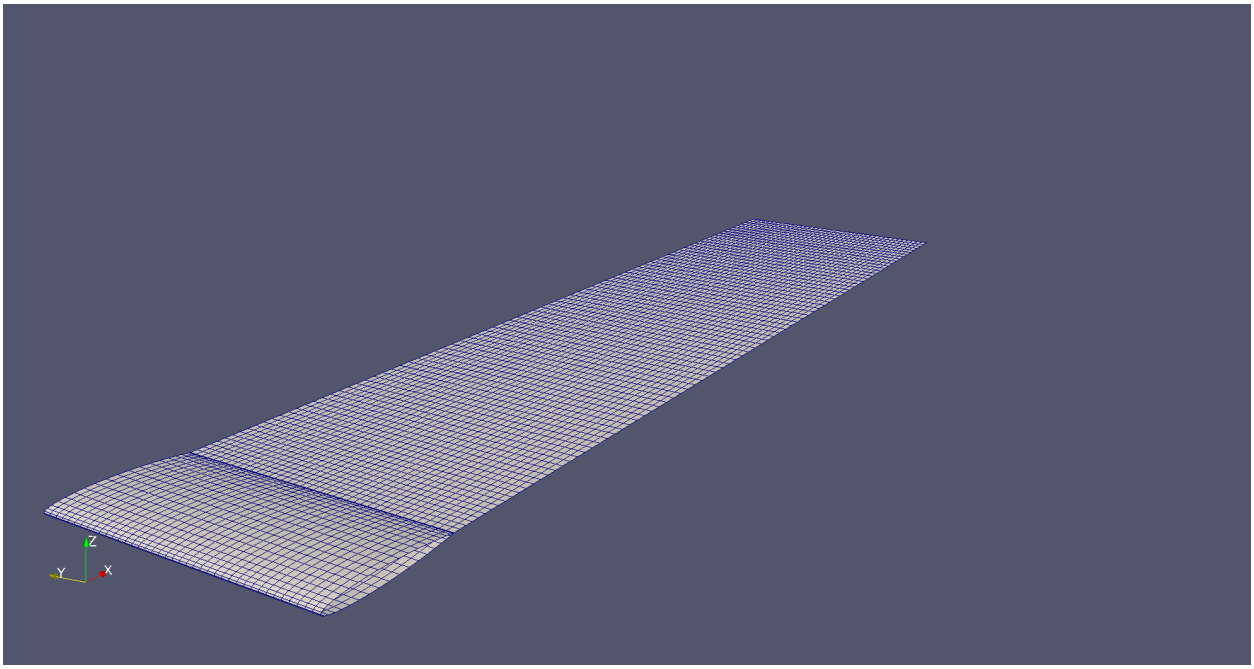

Figure 4.5: Body and wake panels for medium numerical simulation, angle of attack zero

4.2 Van de Vooren Airfoil in Uniform Flow

To verify that the implementation of the Kutta condition produces the correct results we will compare the numerical results obtained using the methods presented in this report with 2D results from the analytical solution of flow around a planar, Van de Vooren airfoil [5]. Results will be compared at several angles of attack, illustrating convergence to the analytical solution with respect to panel resolution, and the number of wake panels. Because we will be comparing 3D numerical results with 2D analytical results we will also illustrate the differences between a 2D solution and a 3D solution with a finite wing span, showing convergence to the 2D solution as the span increases.

First, we will examine the convergence of the numerical solution to the analytical results as the the number of panels on the foil increases. Figure 4.6 shows the velocity magnitude on the foil surface (angle of attack = zero) for the 2D analytical solution, plotted with results from coarse, medium, and fine 3D numerical simulations. The coarse, medium, and fine numerical solutions have 10x20, 20x40 and 40x80 panels on the upper and lower faces of the planar foil, respectively. The planar foil in the numerical solutions has a span/chord ratio of approx. 2. The number of streamwise panels used to model the wake for the coarse, medium, and fine discretizations was 40, 80 and 160 respectively. Figure 4.5 shows the body and wake panels for the medium case.

Upon examination of figure 4.6 we notice that the numerical results converge very quickly, such that the medium and fine results nearly overlap. The most noticeable errors are seen near the leading and trailing edges but these reduce as the number of chordwise panels

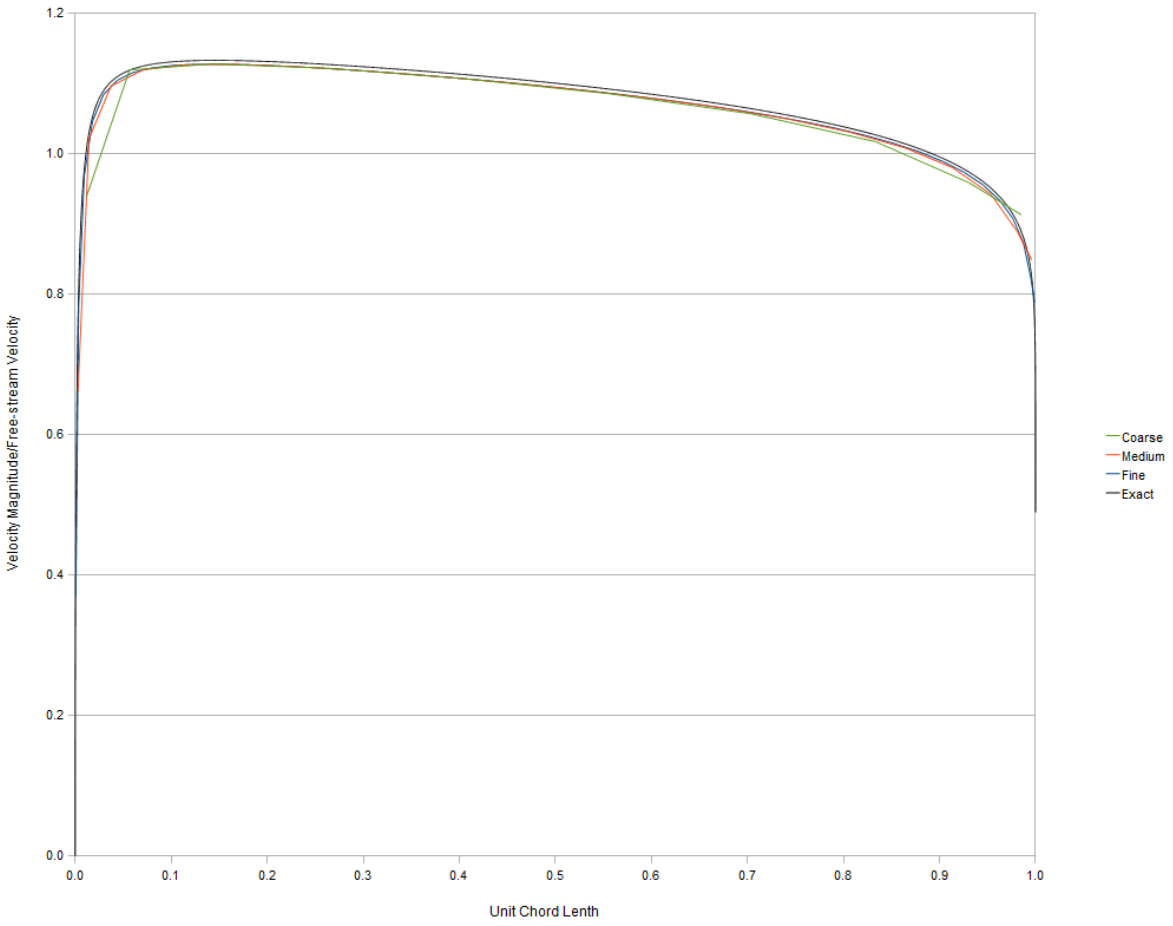

Figure 4.6: Velocity Magnitude on surface of foil for coarse, medium and fine simulations

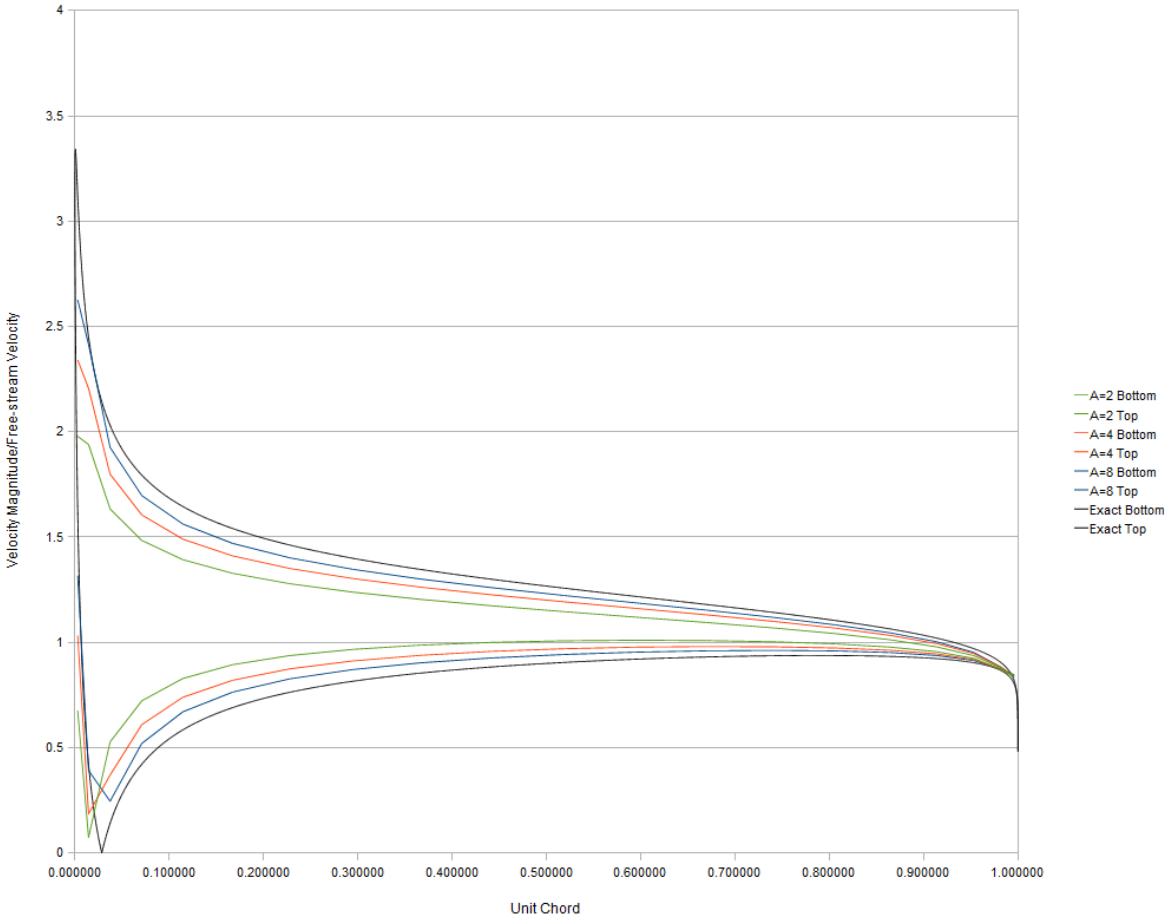

Figure 4.7: Velocity Magnitude on surface of foil for a range of span/chord ratios

increases and the geometric approximations improve in these regions of high curvature. However, we also note the failure of the 3D numerical results to converge to the 2D analytical solution due to the 3D effects at the ends of the planar foil body.

The end effects seen in Figure 4.6 are quite small, however as the angle of attack increases 3D end effects become more noticeable. Figure 4.7 shows 3D numerical and 2D analytical results for the same airfoil pictured in figure 4.5, but with an angle of attack of 10 degrees. Numerical results are shown for planar foils with aspect ratios (span/chord) of 2, 4, and 8. The panels on each of these planar foils were the same size as was used in the fine discretization with zero angle of attack and the results were again taken at the spanwise midpoint. Thus figure 4.7 shows us the rate at which the 3D numerical results converge to the 2D analytical results as the foil end effect is moved farther away from the point of interest. Figure 4.7 also shows that those end effects can be significant when comparing the numerical and analytical results.

We have seen that 3D end effects can significantly affect the results at the midspan of a lifting planar foil. Because those end effects are proportional to angle of attack of the foil, we

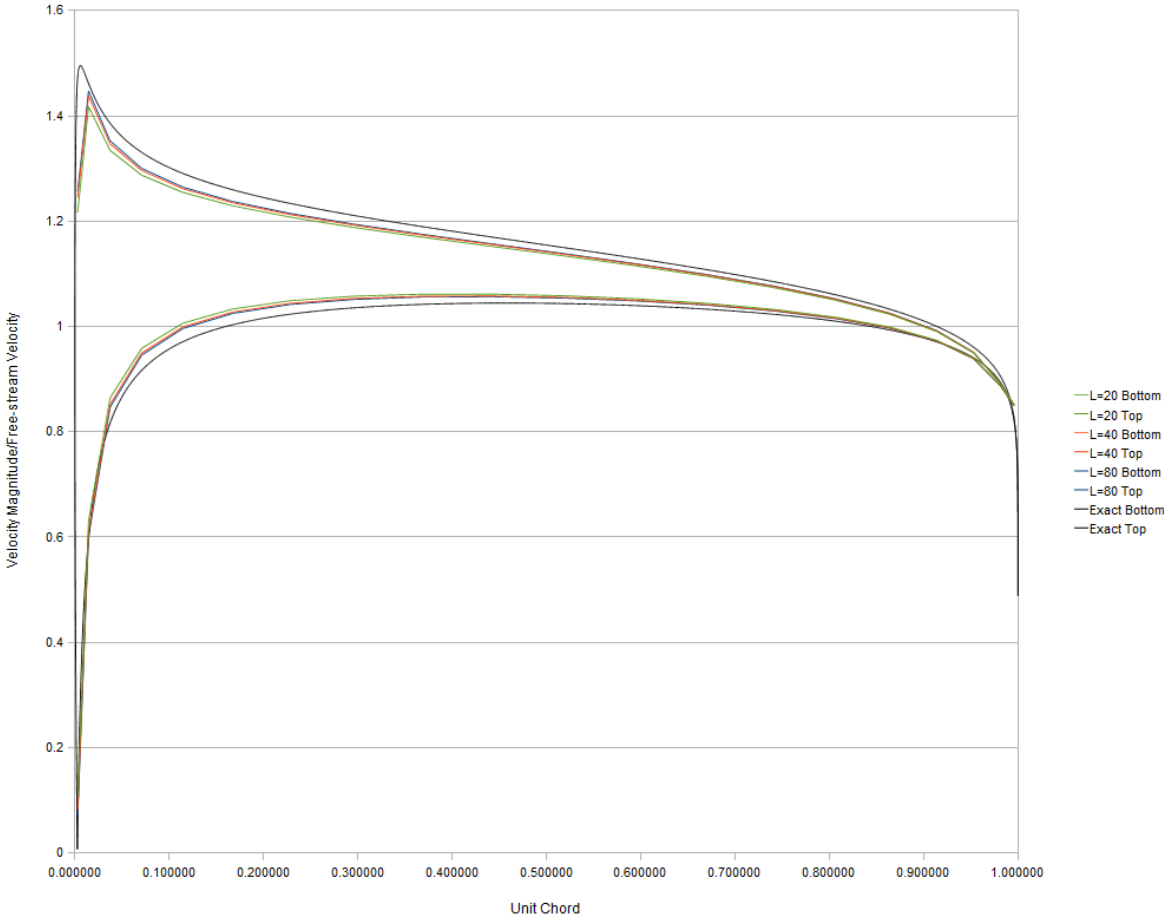

Figure 4.8: Velocity Magnitude on surface of foil for 20, 40, and 80 wake panels

use a more modest angle of attack to study the effect that the length of the modeled wake has on the velocities at the blade surface. Figure 4.8 shows the velocity magnitude on the surface of the same foil at a 3 degree angle of attack. The panel size is again the same as was used in the fine discretization with zero angle of attack and the aspect ratio of the foil was kept at 8 to reduce the end effect errors. The number of streamwise panels used to model the wake has been varied while the aspect ratio of the panels has been kept constant, thus changing the length of the modeled wake. Numerical simulations were performed with 20, 40 and 80 wake panels. From figure 4.8 we can see that the majority of the wake influence comes from the panels near the trailing edge and that variations in the length of the wake have little effect on the results.

5 Validation

In this chapter we will simulate the flow around a Wageningen B-Series propeller at several advance ratios and compare the thrust and torque predicted by the numerical simulation to the published experimental results for the B-Series [11] [7].

5.1 B-Series Propellers

The Wageningen B-Series propellers were chosen for this validation effort because the experimental results are well known to the marine community and because the data was readily available. The series represents a set of propellers with four to seven blades, with a range of expanded area ratios from 0.45 - 1.05 and a range of pitch-diameter ratios from 0.5 - 1.4. Experimentally measured thrust, and torque coefficients have been published for advance ratios from 0.0 - 1.6. Advance ratio, thrust coefficient and torque coefficient are of the forms noted in Chapter 3.

The geometry of the propellers simulated in this report has been recreated from tables of shape parameters published in [11] and [7].

5.2 Propeller Forces

The flow around a five bladed propeller with an expanded area ratio of 1.05 and a pitch-diameter ratio of 0.8, acting in an otherwise uniform flow, was simulated for comparison with the published experimental data. A range of advance ratios (0.3-0.6) were simulated to evaluate the numerical predictions at several propeller loading conditions. Simulations were performed for four discretizations of the blade, hub and wake surfaces. Figures 5.1 - 5.4 illustrate the panels for these coarse, medium, fine, and xfine simulations. Table 5.1 lists the number of panels on the blade in the chordwise and spanwise directions, as well as the number of streamwise panels used to model the wake. One can see from figures 5.1 - 5.4 that in each of the simulations the wake extends approximately one revolution downstream.

Figures 5.5 and 5.6 plot the thrust and torque coefficients from the numerical simulation along with the published B-Series data. In figure 5.5 we see that the numerically predicted thust coefficient is greater than the experimentally predicted values for all advance ratios and discretizations. This could be expected from an inviscid, irrotational model, which fails to model phenomena such as separation, however the differences of this magnitude will likely

	N_S	N_C	L
Coarse	5	5	28
Med	7	7	40
Fine	10	10	56
xFine	14	14	80

Table 5.1: Number of panels for the coarse, medium, fine and xfine simulations

restrict the usage the numerical model in it's present state. These differences may be due to the inviscid and irrotational assumptions in the physical model, however results published by Hoshino [2] for a similar physical model achieved better results.

We also notice that the slope of the numerically predicted K_T curves is less than that of the B-Series values; indicating that the numerical method predicts a more constant development of thrust over variations in advance ratio than is seen in the experimental data. This difference between the slopes of the numerical and experimental curves could be caused by several of the assumptions made in the physical model, including: the application of the kutta condition at highly loaded blade sections, or the lack of a model for the blade tip vortex.

In figure 5.6, which plots the K_Q curves, we again see that the slope of the numerically predicted results is less than that of the experimental results. Torque is highly affected by the induced velocities from the blade tip vortex and the incomplete modeling of that vortex in the method proposed in this report could contribute to the insensitivity of the K_Q curves to changes in advance ratio.

Also, in figure 5.6 we see that the torque coefficient reduces as the grid resolution increases; starting above the experimental results in the Coarse case but falling to below the experimental results in the xFine case; not converging to the experimental results. It is important to note that in the plots of both K_T and K_Q that the difference between the numerical values for any two discretizations does not appear to decrease as the panels become smaller. This inability to converge, even to results other that the experimental results, could be due to the inadequacies in the physical model mentioned above or to an improper numerical implementation of the continuum equations. In any case, the lack of observed convergence as the panel size is decreased is a problem which must be corrected prior to extensive use of the code.

Colored contour plots of the velocity magnitude and pressure coefficient for the coarse, medium, fine and xfine cases, for advance ratios 0.3-0.6 are given in the Appendix.

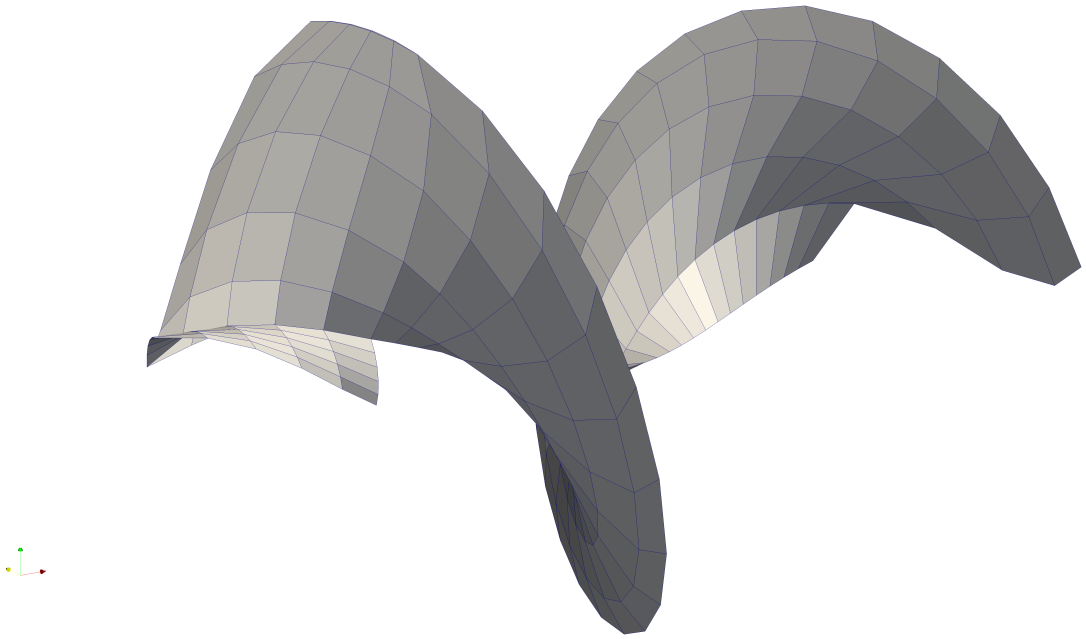

Figure 5.1: Panels for coarse simulation, $N_S = N_C = 5$

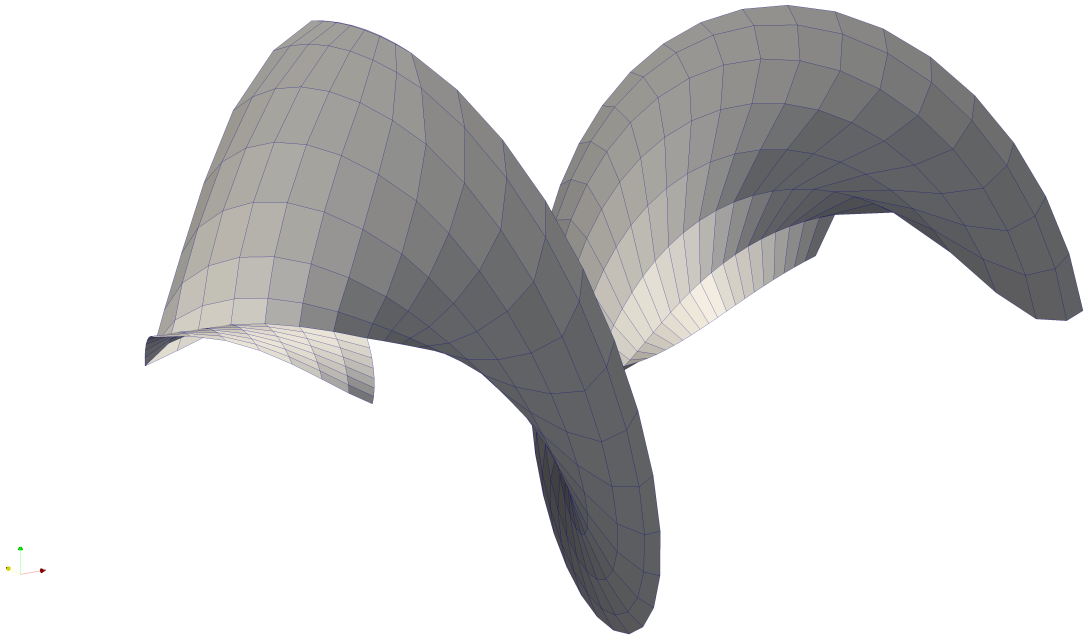

Figure 5.2: Panels for medium simulation, $N_S = N_C = 7$

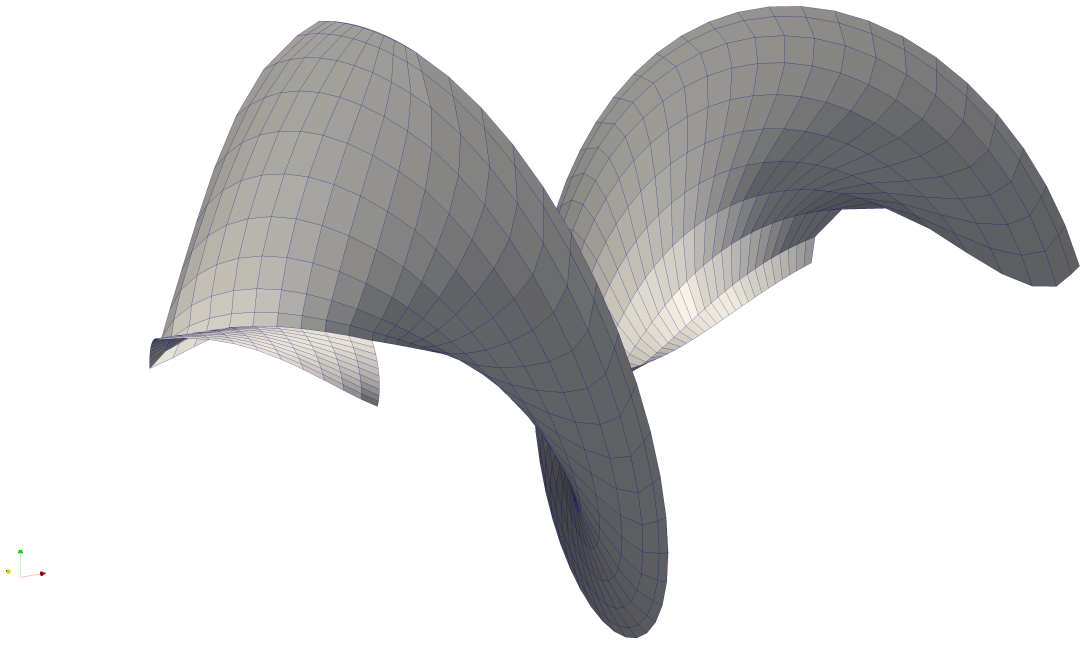

Figure 5.3: Panels for fine simulation, $N_S = N_C = 10$

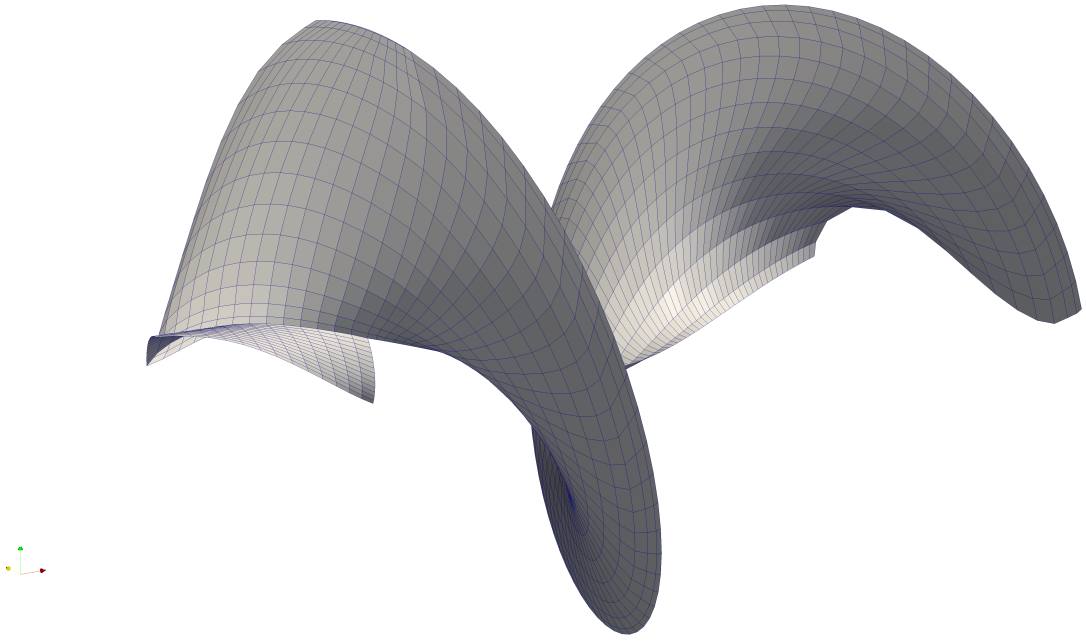

Figure 5.4: Panels for xfine simulation, $N_S = N_C = 14$

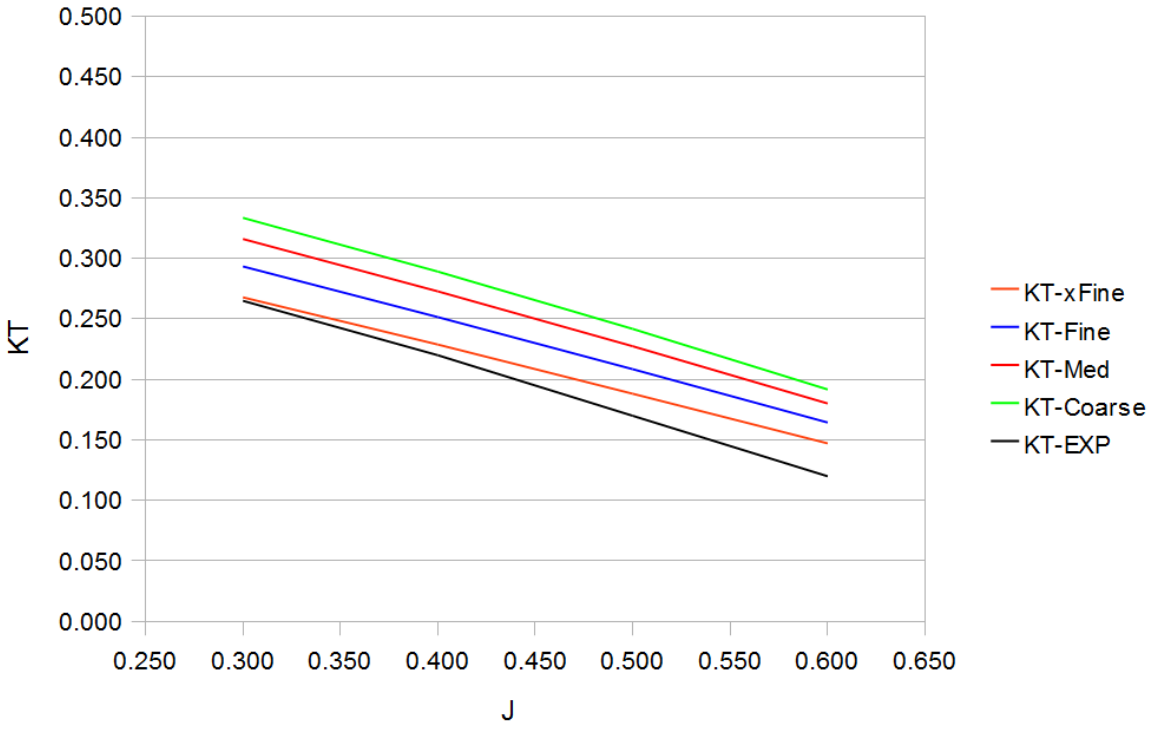

Figure 5.5: K_T curves for B5-105, $P/D = 0.8$

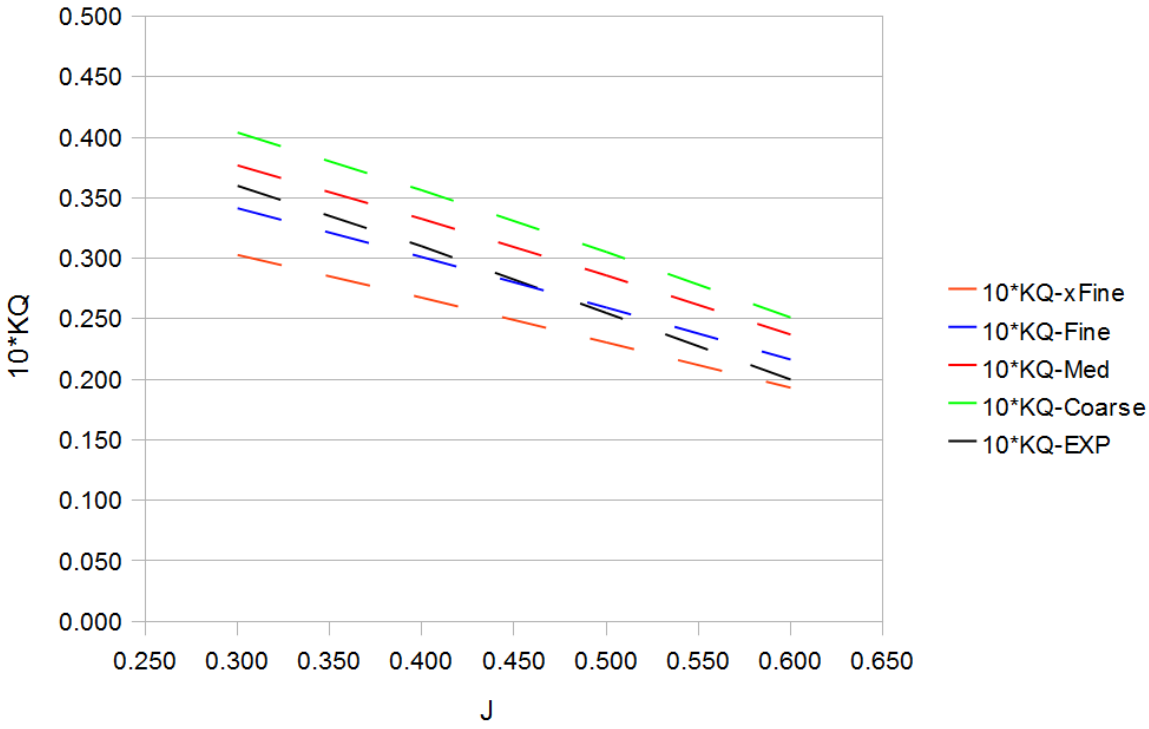

Figure 5.6: K_Q curves for B5-105, $P/D = 0.8$

6 Conclusions

This report describes the governing equation, and boundary conditions for a marine propeller operating in a uniform flow field of inviscid and irrotational fluid and a method is presented by which the velocity and pressure on the blade surface of the propeller can be numerically simulated. The method has been tested on several geometries including a sphere, a planar Van de Vooren airfoil, and a Wageningen B-Series propeller.

The numerical results compared well with the anylitical results for both the sphere and the Van der Vooren airfoil in potential flow, however significant differences were seen when compared to the experimentally measured thrust and torque coefficients for the B-Series propeller. Most troubling is that neither the numerical results for thrust of torque on the B-Series propeller we observed to converge to as the panel size on the computational surfaces was decreased.

Results published by Hoshino [2] show a more favorable comparison with experiemental data, however no grid convergence tests with respect to thrust and torque values were provided in [2]. Other applications of boundary element or panel methods suggests that this type of simulation can provide accurate predictions of the steady thrust and torque on a marine propeller [3].

Further research into the modeling of wake roll-up [6] and the blade tip vortex could improve the comparison with experimental data.

Bibliography

[1] J. Hess. Calculation of potential flow about arbitrary three-dimensional lifting bodies. Technical report, Naval Air Systems Command Report, 1972.

[2] T. Hoshino. Hydrodynamic analysis of propellers in steady flow using a surface panel method. *Journal of The Society of Naval Architects of Japan*, 165:55–70, 1989.

[3] Ching-Yeh Hsin. Development and analysis of panel methods for propellers in unsteady flow. Technical report, Massachusetts Institute of Technology, 1990.

[4] Ching-Yeh Hsin. A panel method for the analysis of the flow around highly skewed propellers. Technical report, Sea Grant College Program, Massachusetts Institute of Technology, 1991.

[5] J. Katz. *Low-Speed Aerodynamics: From Wing Theory to Panel Methods*. McGraw-Hill, New York, NY, 1991.

[6] Robert Krasny. Computation of vortex sheet roll-up in the trefftz plane. *Journal of Fluid Mechanics*, 184:123–155, 1987.

[7] G. Kuiper. The wageningen propeller series. Technical report, Maritime Research Institute, Netherlands, 1992.

[8] Chang-Sup Lee. Prediction of steady and unsteady performance of marine propellers with or without cavitation by numerical lifting-surface theory. Technical report, Massachusetts Institute of Technology, 1979.

[9] Edward V. Lewis. *Principles of Naval Architecture, Volume II*. Society of Naval Architects and Marine Engineers, Jersey City, NJ, 1988.

[10] L. Morino. Steady and oscillatory subsonic and supersonic aerodynamics around complex configurations. *AIAA Journal*, 13:368–374, 1974.

[11] M.W.C Oosterveld. Further computer-analyzed data of the wageningen b-screw series. *Shipbuilding and Marine Engineering Monthly*, 22, 1975.

[12] Shin H. Rhee. Cfd validation for a marine propeller using an unstructured mesh based rans method. *Proceedings of ASME FEDSM'03*, 2003.

A Appendix

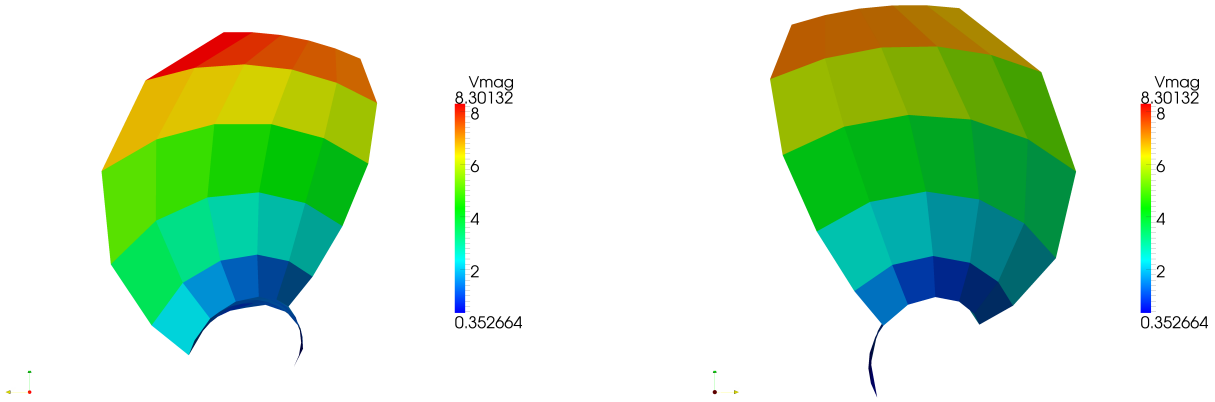

Figure A.1: Velocity Magnitude for B5-105, Coarse, $P/D = 0.8$, $J = 0.3$ suction side (left) and pressure side (right)

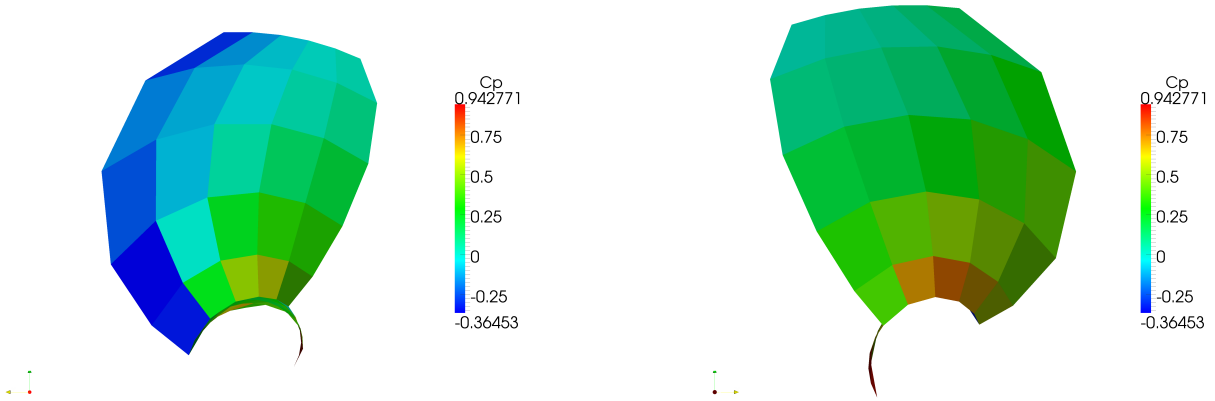

Figure A.2: C_P for B5-105, Coarse, $P/D = 0.8$, $J = 0.3$ suction side (left) and pressure side (right)

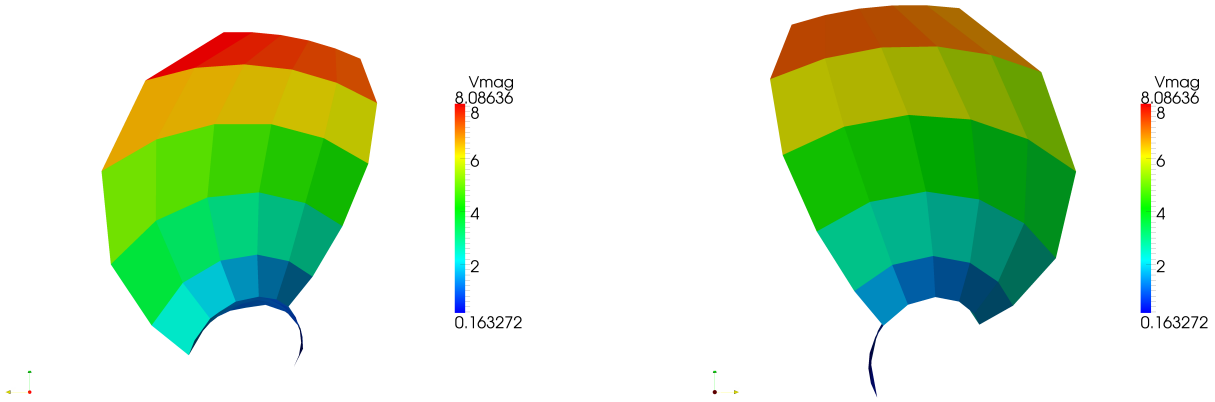

Figure A.3: Velocity Magnitude for B5-105, Coarse, $P/D = 0.8$, $J = 0.4$ suction side (left) and pressure side (right)

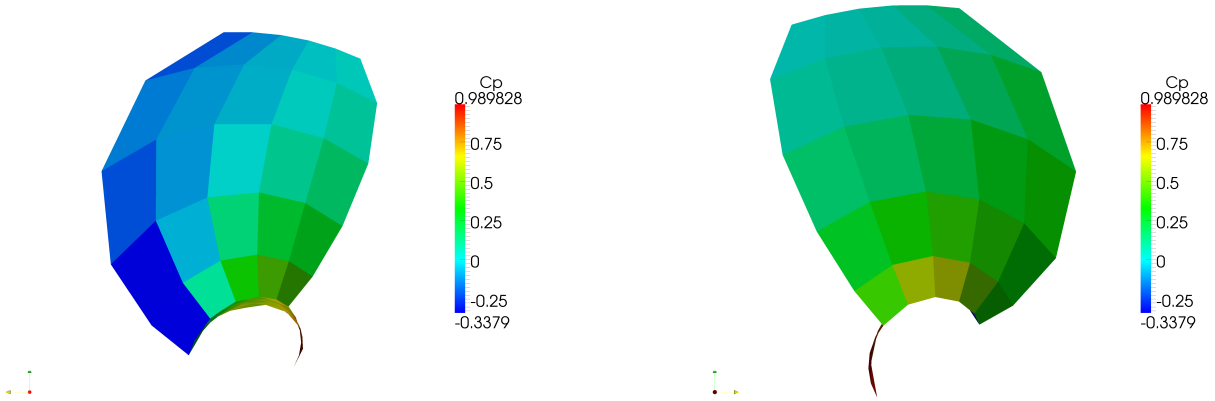

Figure A.4: C_P for B5-105, Coarse, $P/D = 0.8$, $J = 0.4$ suction side (left) and pressure side (right)

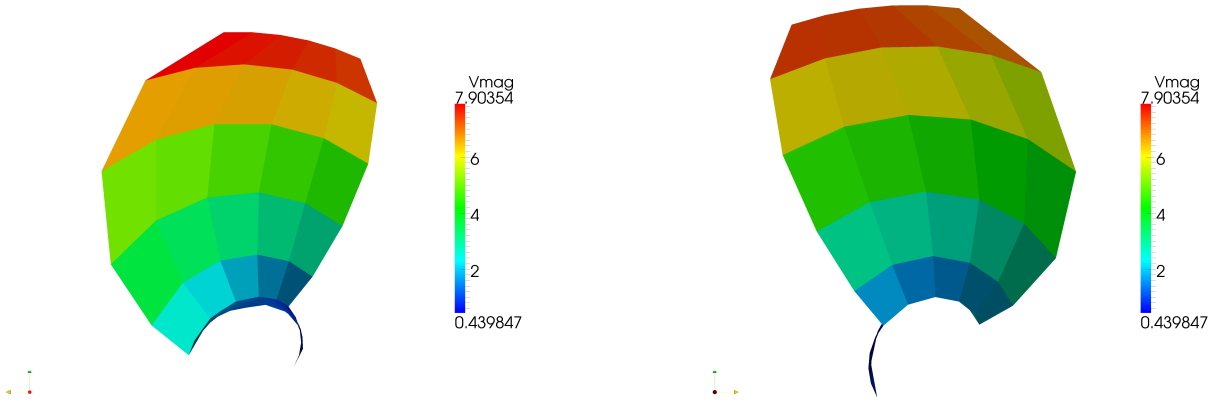

Figure A.5: Velocity Magnitude for B5-105, Coarse, $P/D = 0.8$, $J = 0.5$ suction side (left) and pressure side (right)

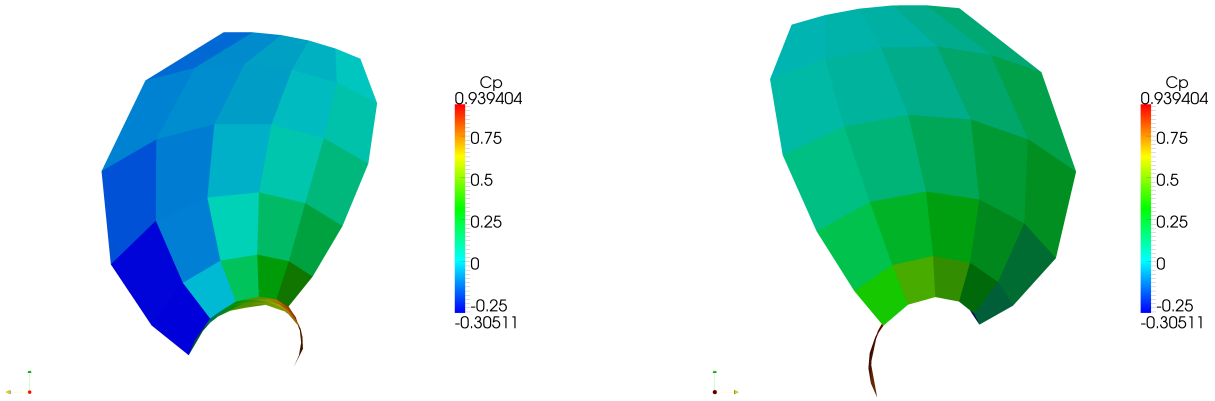

Figure A.6: C_P for B5-105, Coarse, $P/D = 0.8$, $J = 0.5$ suction side (left) and pressure side (right)

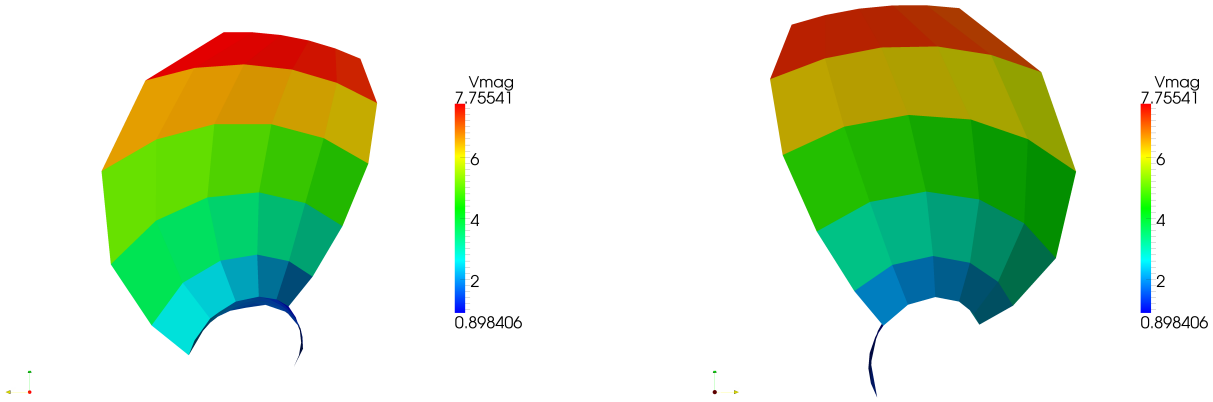

Figure A.7: Velocity Magnitude for B5-105, Coarse, $P/D = 0.8$, $J = 0.6$ suction side (left) and pressure side (right)

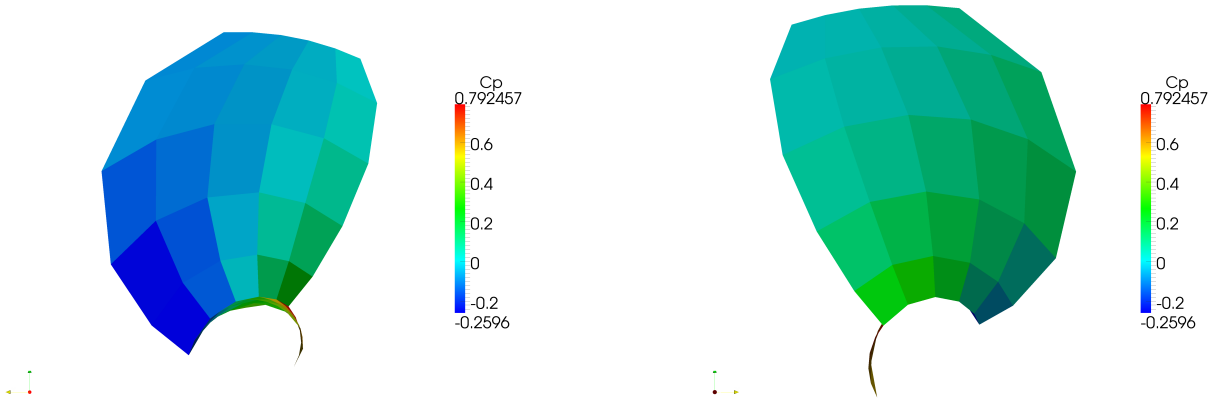

Figure A.8: C_P for B5-105, Coarse, $P/D = 0.8$, $J = 0.6$ suction side (left) and pressure side (right)

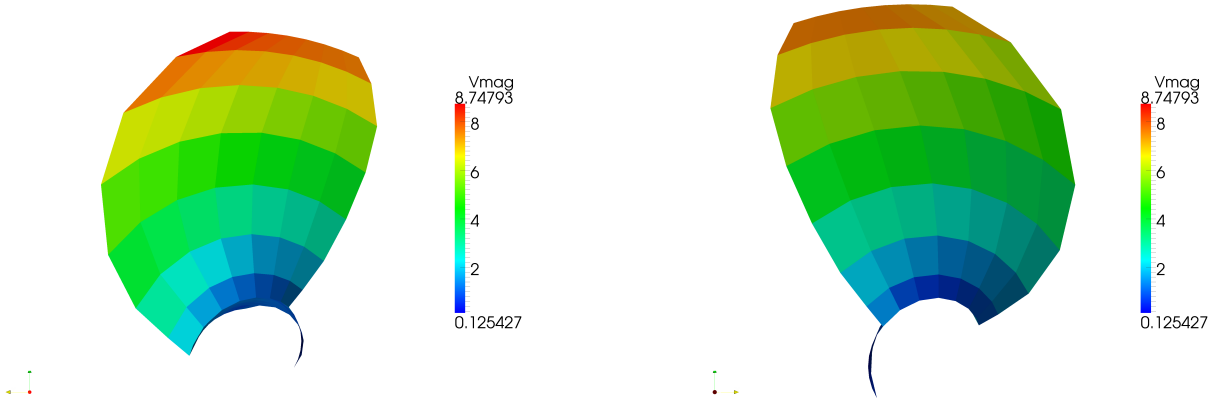

Figure A.9: Velocity Magnitude for B5-105, Medium, $P/D = 0.8$, $J = 0.3$ suction side (left) and pressure side (right)

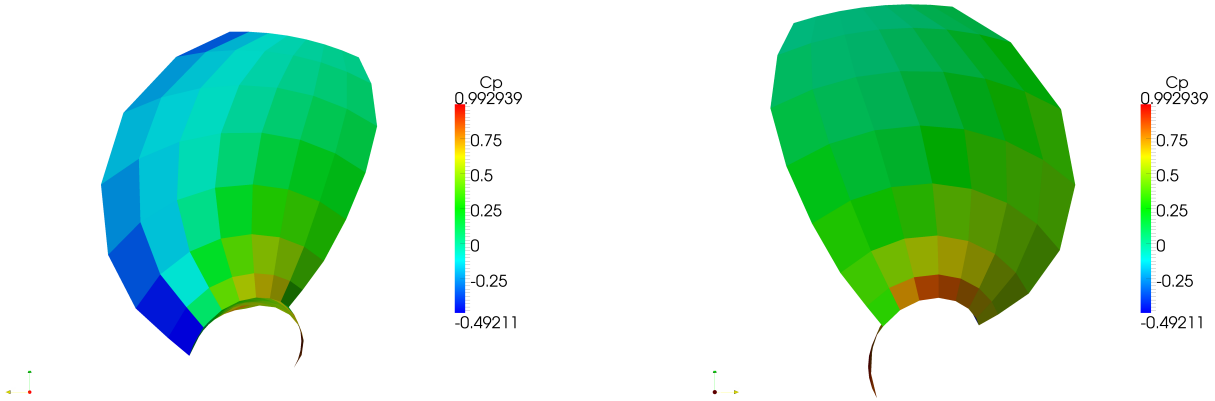

Figure A.10: C_P for B5-105, Medium, $P/D = 0.8$, $J = 0.3$ suction side (left) and pressure side (right)

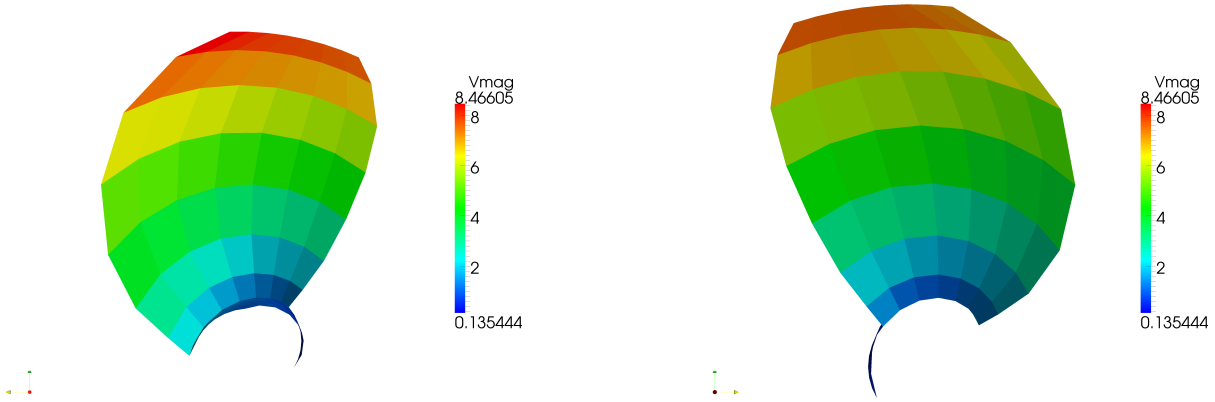

Figure A.11: Velocity Magnitude for B5-105, Medium, $P/D = 0.8$, $J = 0.4$ suction side (left) and pressure side (right)

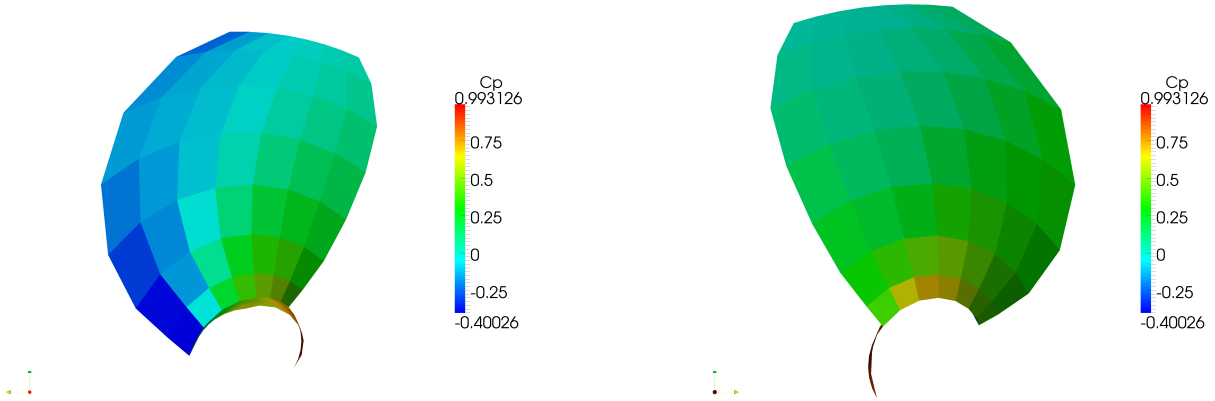

Figure A.12: C_P for B5-105, Medium, $P/D = 0.8$, $J = 0.4$ suction side (left) and pressure side (right)

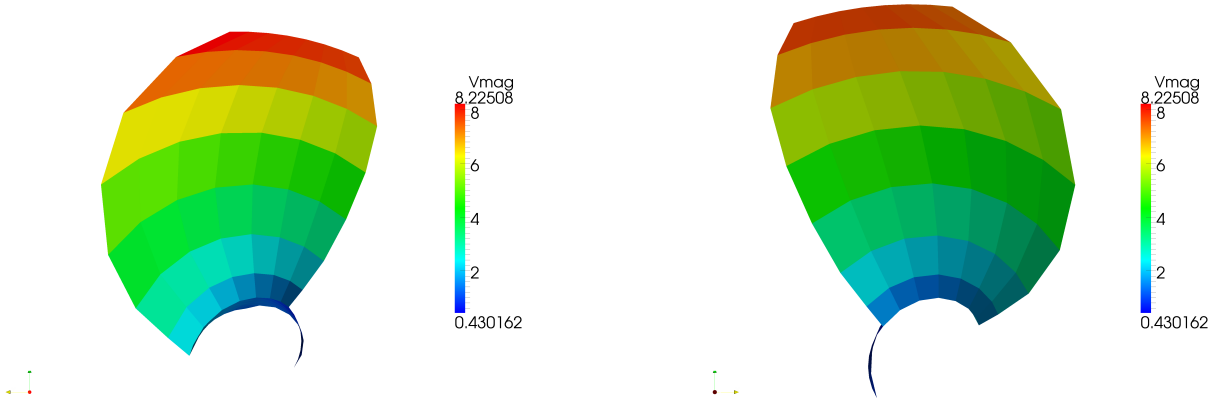

Figure A.13: Velocity Magnitude for B5-105, Medium, $P/D = 0.8$, $J = 0.5$ suction side (left) and pressure side (right)

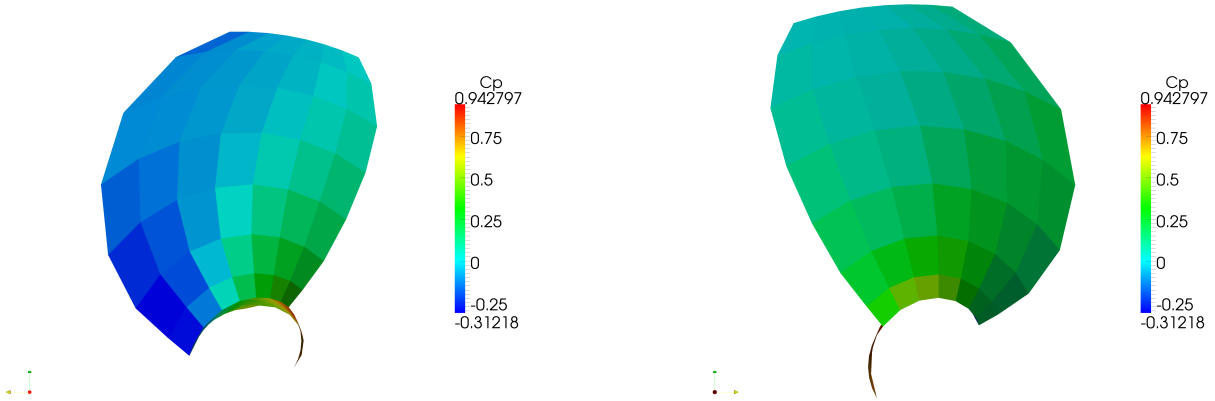

Figure A.14: C_P for B5-105, Medium, $P/D = 0.8$, $J = 0.5$ suction side (left) and pressure side (right)

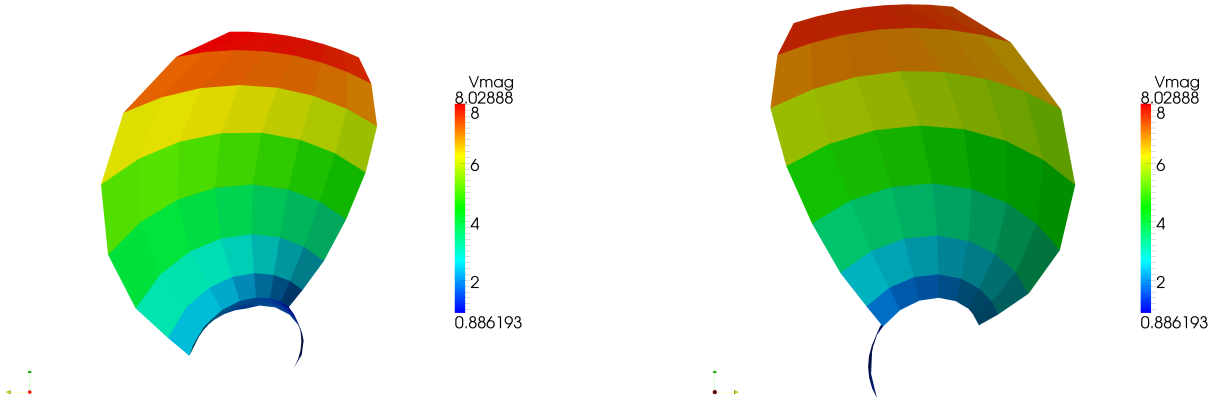

Figure A.15: Velocity Magnitude for B5-105, Medium, $P/D = 0.8$, $J = 0.6$ suction side (left) and pressure side (right)

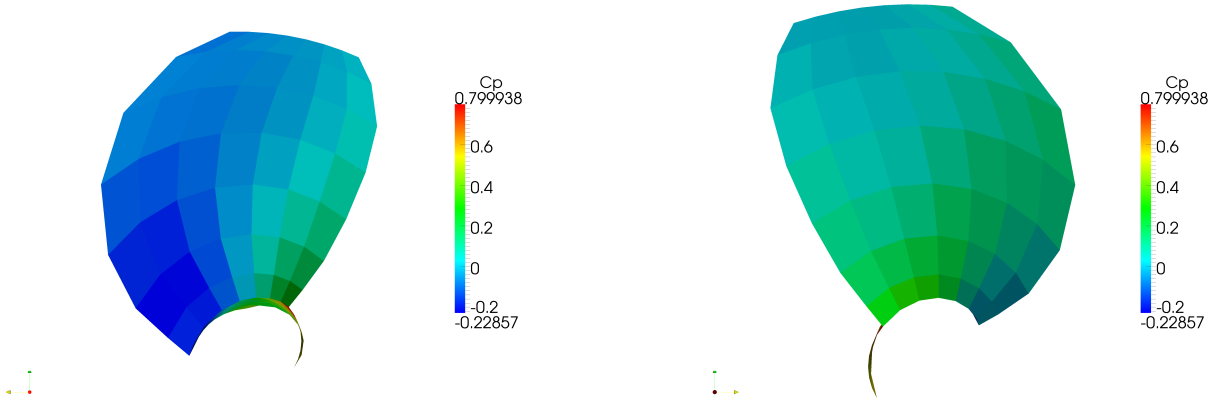

Figure A.16: C_P for B5-105, Medium, $P/D = 0.8$, $J = 0.6$ suction side (left) and pressure side (right)

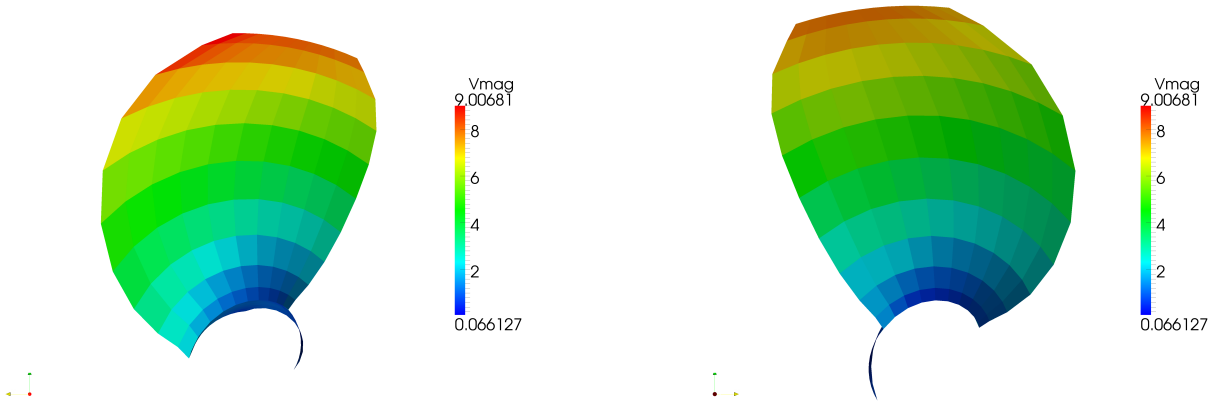

Figure A.17: Velocity Magnitude for B5-105, Fine, $P/D = 0.8$, $J = 0.3$ suction side (left) and pressure side (right)

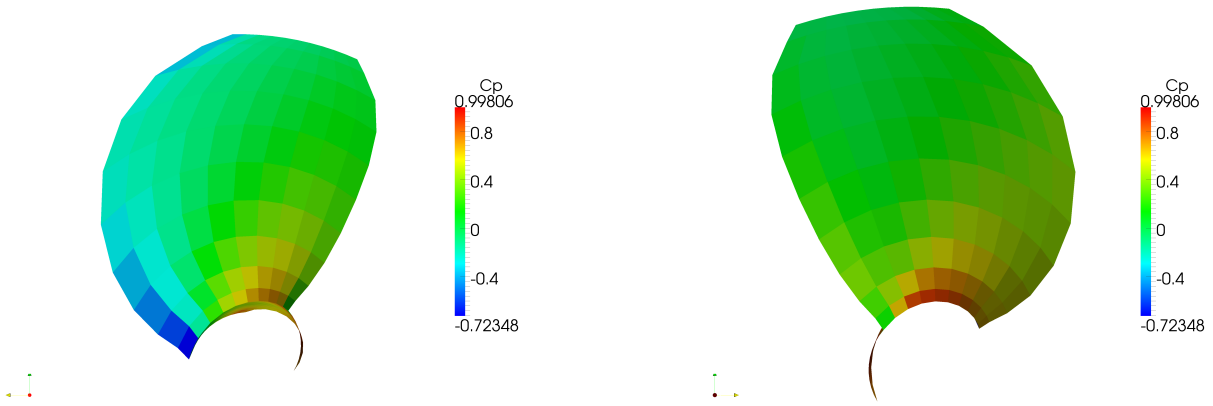

Figure A.18: C_P for B5-105, Fine, $P/D = 0.8$, $J = 0.3$ suction side (left) and pressure side (right)

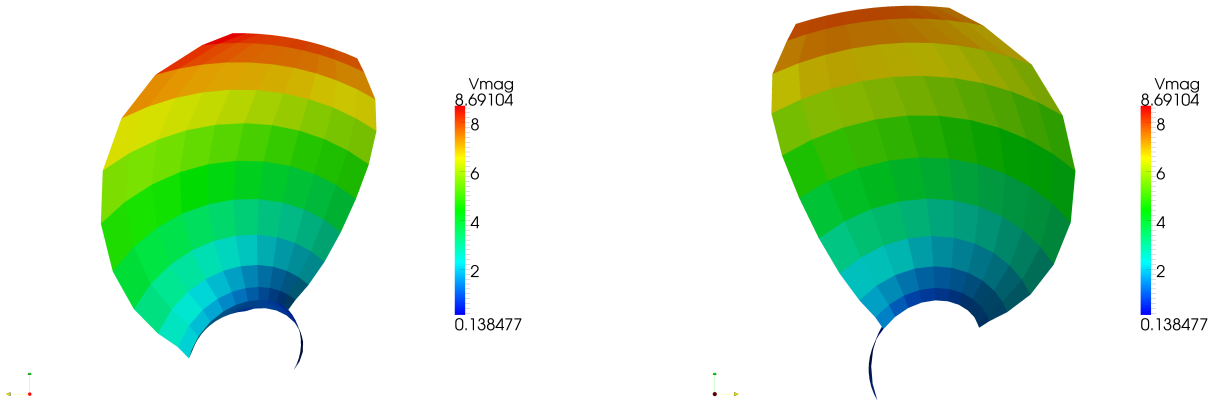

Figure A.19: Velocity Magnitude for B5-105, Fine, $P/D = 0.8$, $J = 0.4$ suction side (left) and pressure side (right)

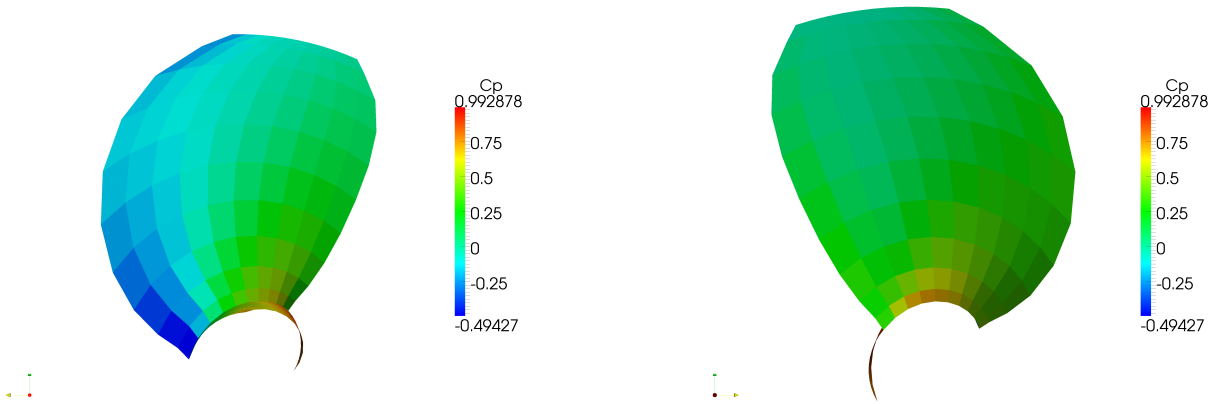

Figure A.20: C_P for B5-105, Fine, $P/D = 0.8$, $J = 0.4$ suction side (left) and pressure side (right)

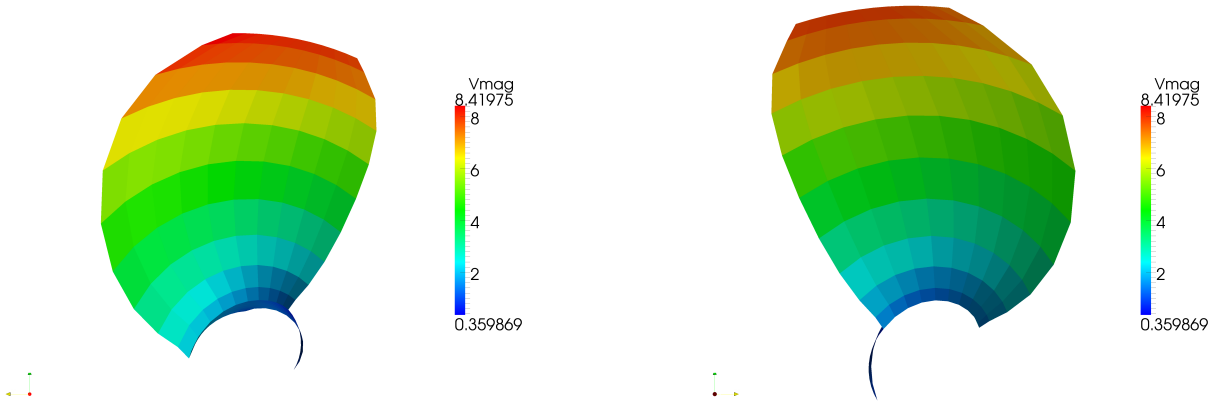

Figure A.21: Velocity Magnitude for B5-105, Fine, $P/D = 0.8$, $J = 0.5$ suction side (left) and pressure side (right)

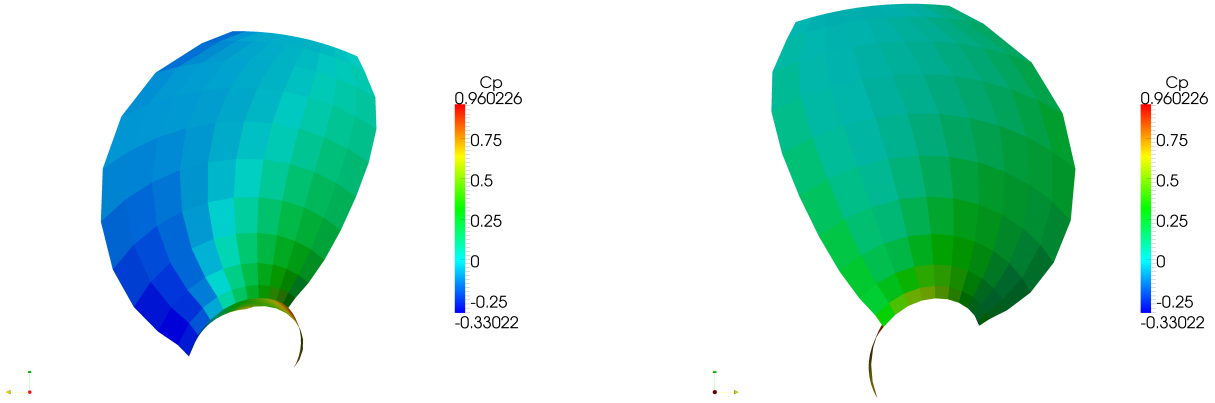

Figure A.22: C_P for B5-105, Fine, $P/D = 0.8$, $J = 0.5$ suction side (left) and pressure side (right)

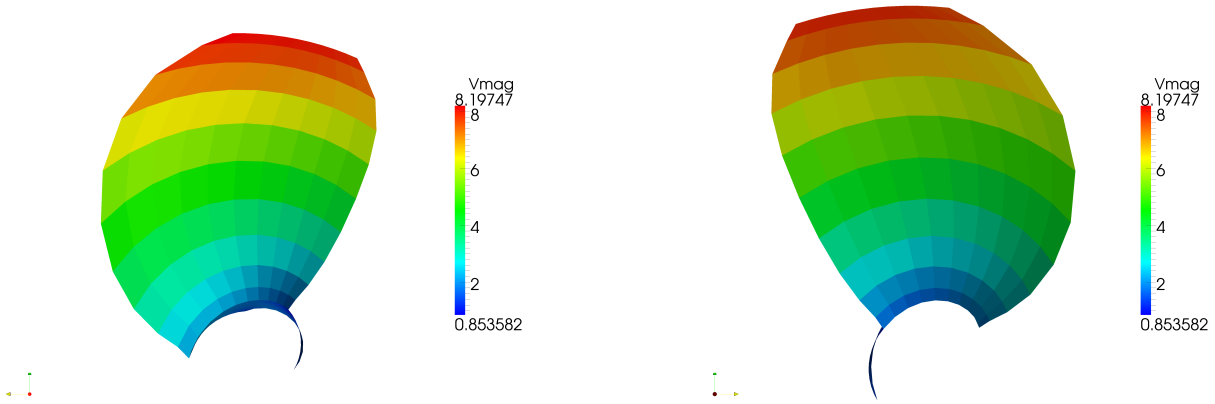

Figure A.23: Velocity Magnitude for B5-105, Fine, $P/D = 0.8$, $J = 0.6$ suction side (left) and pressure side (right)

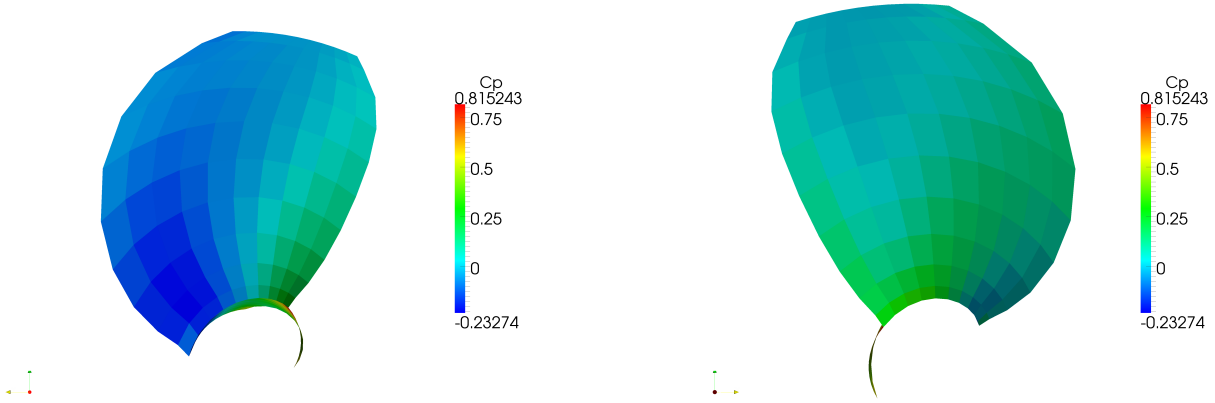

Figure A.24: C_P for B5-105, Fine, $P/D = 0.8$, $J = 0.6$ suction side (left) and pressure side (right)

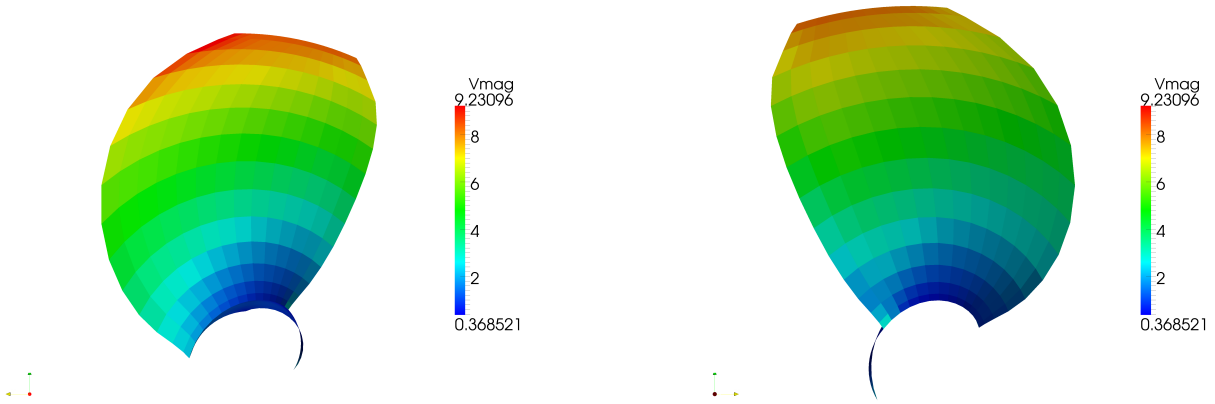

Figure A.25: Velocity Magnitude for B5-105, xFine, $P/D = 0.8$, $J = 0.3$ suction side (left) and pressure side (right)

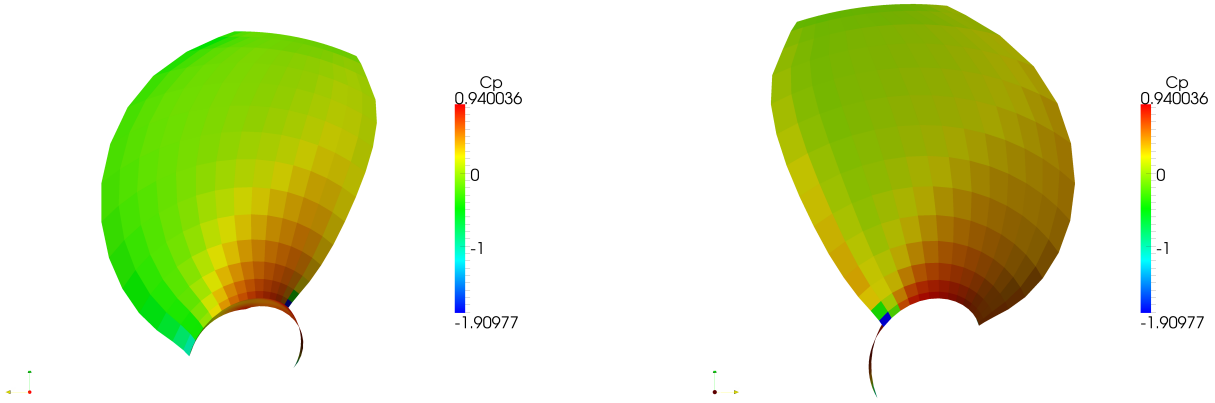

Figure A.26: C_P for B5-105, xFine, $P/D = 0.8$, $J = 0.3$ suction side (left) and pressure side (right)

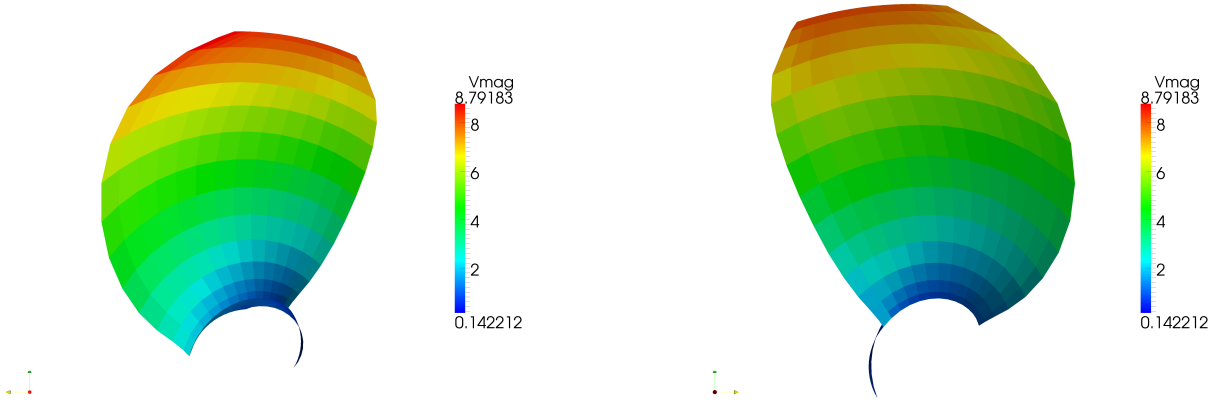

Figure A.27: Velocity Magnitude for B5-105, xFine, $P/D = 0.8$, $J = 0.4$ suction side (left) and pressure side (right)

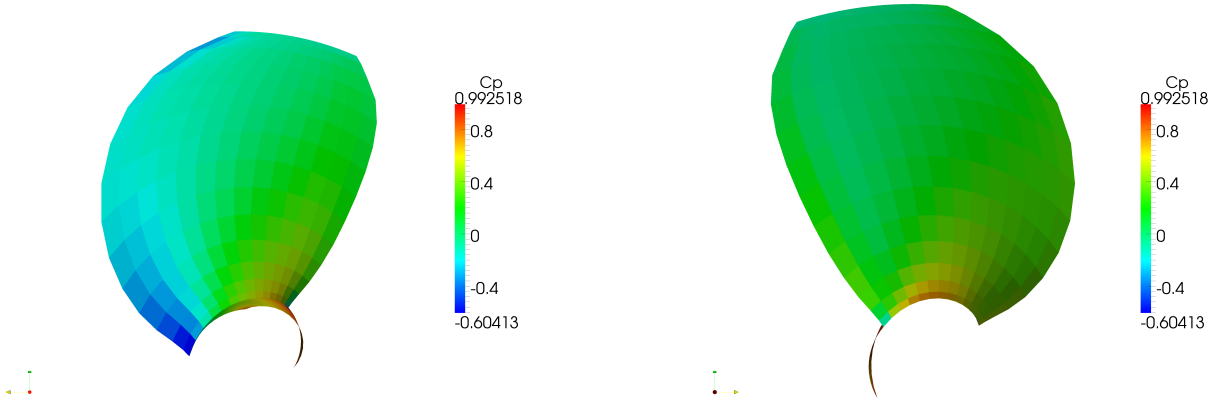

Figure A.28: C_P for B5-105, xFine, $P/D = 0.8$, $J = 0.4$ suction side (left) and pressure side (right)

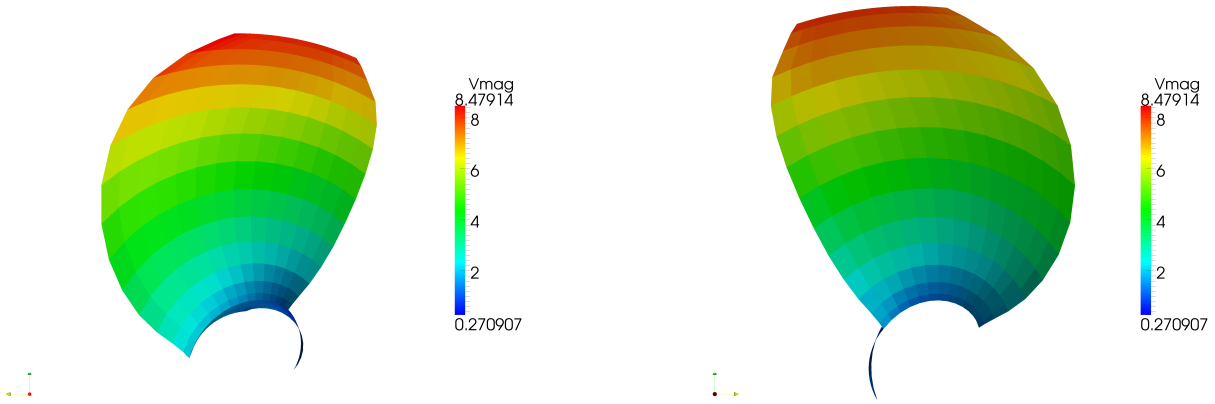

Figure A.29: Velocity Magnitude for B5-105, xFine, $P/D = 0.8$, $J = 0.5$ suction side (left) and pressure side (right)

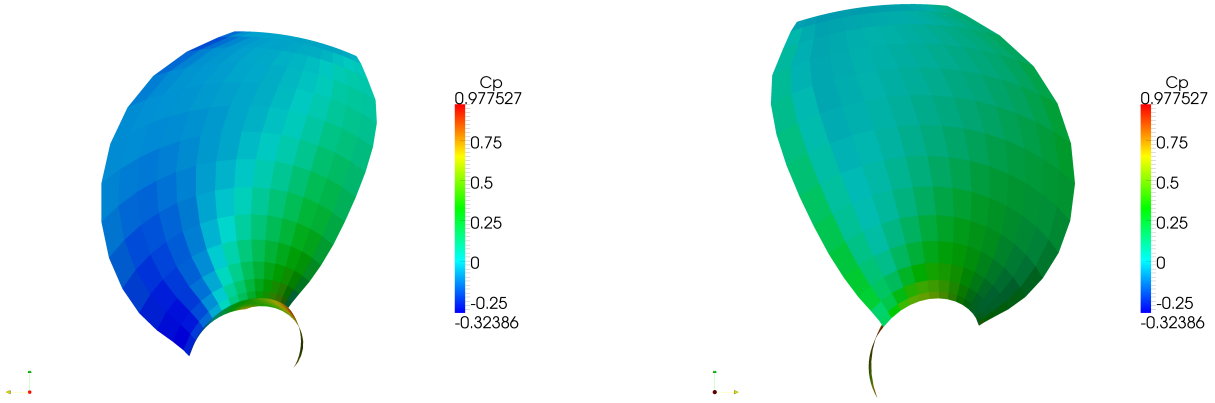

Figure A.30: C_P for B5-105, xFine, $P/D = 0.8$, $J = 0.5$ suction side (left) and pressure side (right)

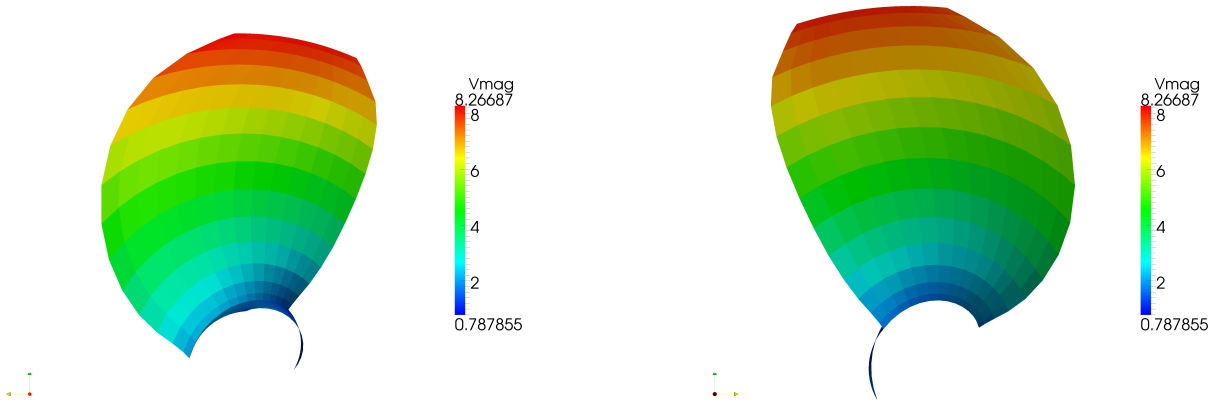

Figure A.31: Velocity Magnitude for B5-105, xFine, $P/D = 0.8$, $J = 0.6$ suction side (left) and pressure side (right)

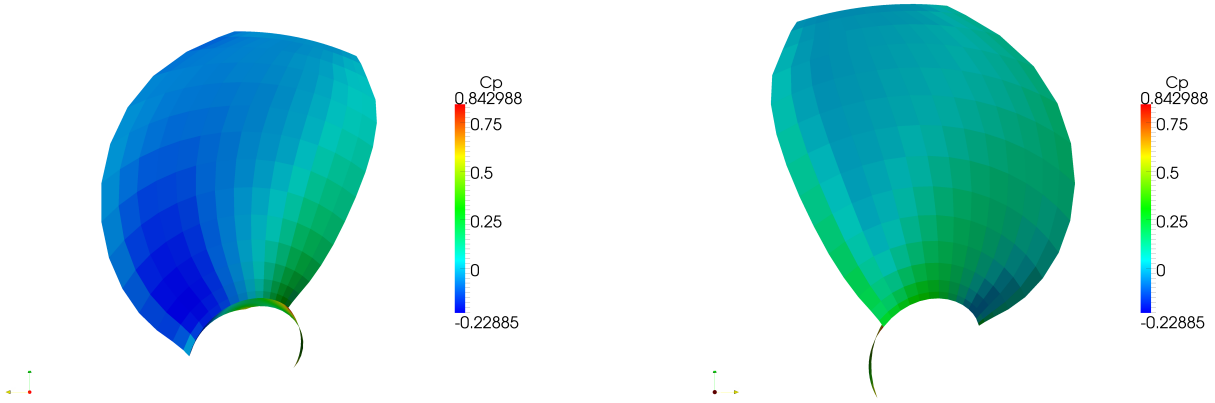

Figure A.32: C_P for B5-105, xFine, $P/D = 0.8$, $J = 0.6$ suction side (left) and pressure side (right)

Vita

The author was born in Richmond, Virginia. He obtained his Bachelor's degree in naval architecture and marine engineering from the University of New Orleans in 2006. Upon graduation, he began working at Northrop Grumman's Avondale, LA facility as a Naval Architect, in their research and development department. Greg lives with his wife Katie and their chihuahua Tchopitoulas in New Orleans, LA.